

Possible contribution of X-ray binary jets to the Galactic cosmic ray and neutrino flux

D. Kantzas,^{1,2,3}★ S. Markoff,^{2,3} A. J. Cooper,^{4,2} D. Gaggero,⁵ M. Petropoulou^{6,7} & P. De La Torre Luque⁸

¹Laboratoire d'Annecy-le-Vieux de Physique Théorique (LAPTh), CNRS, USMB, F-74940 Annecy, France

²Anton Pannekoek Institute for Astronomy (API), University of Amsterdam, Science Park 904, 1098 XH Amsterdam, the Netherlands

³GRavitational AstroParticle Physics Amsterdam (GRAPPA), University of Amsterdam, Science Park 904, 1098 XH Amsterdam, the Netherlands

⁴Astrophysics, The University of Oxford, Keble Road, Oxford OX1 3RH, UK

⁵INFN Sezione di Pisa, Polo Fibonacci, Largo B. Pontecorvo 3, 56127 Pisa, Italy

⁶Department of Physics, National and Kapodistrian University of Athens, University Campus Zografos, GR 15783, Athens, Greece

⁷Institute of Accelerating Systems & Applications, University Campus Zografos, Athens, Greece

⁸Stockholm University and The Oskar Klein Centre for Cosmoparticle Physics, Alba Nova, 10691 Stockholm, Sweden

Accepted XXX. Received YYY; in original form ZZZ

ABSTRACT

For over a century, the identification of high-energy cosmic ray (CR) sources remains an open question. For Galactic CRs with energy up to 10^{15} eV, supernova remnants (SNRs) have traditionally been thought the main candidate source. However, recent TeV γ -ray observations have questioned the SNR paradigm. Propagating CRs are deflected by the Galactic magnetic field, hence, γ -rays and neutrinos produced via inelastic hadronic interactions are the only means for unveiling the CR sources. In this work, we study the γ -ray and neutrino emission produced by CRs accelerated inside Galactic jets of stellar-mass black holes in X-ray binaries (BHXBs). We calculate the intrinsic neutrino emission of two prototypical BHXBs, Cygnus X–1 and GX 339–4, for which we have high-quality, quasi-simultaneous multiwavelength spectra. Based on these prototypical sources, we discuss the likelihood of the 35 known Galactic BHXBs to be efficient CR accelerators. Moreover, we estimate the potential contribution to the CR spectrum of a viable population of BHXBs that reside in the Galactic plane. When these BHXBs go into outburst, they may accelerate particles up to 100s of TeV that contribute to the diffuse γ -ray and neutrino spectra while propagating in the Galactic medium. Using HERMES, an open-source code that calculates the hadronic processes along the line of sight, we discuss the contribution of BHXBs to the diffuse γ -ray and neutrino fluxes, and compare these to their intrinsic γ -ray and neutrino emissions. Finally, we discuss the contribution of BHXBs to the observed spectrum of Galactic CRs.

Key words: cosmic rays – neutrinos – acceleration of particles

1 INTRODUCTION

For more than a hundred years, the origin of cosmic rays (CRs) has remained an unsolved mystery. CRs are accelerated atomic nuclei of extraterrestrial origin that populate a power law that covers more than ten orders of magnitude in energy. Energetic protons of Galactic origin dominate the low-energy regime of the CR spectrum that shows a break at around 1 PeV (10^{15} eV), known as the “knee”. The CR composition beyond the “knee” is not certain, but it is likely that the CR spectrum becomes dominated by heavier elements at the highest energy regime up to the “ankle” feature at around 1 EeV (10^{18} eV; Buitink et al. 2016; Abreu et al. 2021). Beyond the “ankle”, different experiments favour different CR composition, and it is not clear yet whether CRs are proton or iron dominated (see e.g. Pierre-Auger 2023; TA 2022).

The astrophysical sources capable of accelerating CRs up to (and

beyond) 1 PeV are the so-called PeVatrons. Based on energetic arguments, supernovae (SNe) and young supernova remnants (SNRs) in particular, have so-far been considered the dominant candidate sources of Galactic CRs (Baade & Zwicky 1934; Ginzburg & Syrovatskii 1964; Hillas 1984; Blasi 2013b). When CRs are accelerated in the SN/SNR shock front, they interact with the dense gas clouds to initiate inelastic collisions that will lead to the formation of secondary particles, such as γ -rays and neutrinos (e.g. Stephens & Badhwar 1981; Dermer 1986; Berezhinsky 1991; Mannheim 1993; Mannheim & Schlickeiser 1994; Rachen & Mészáros 1998; Aharonian & Atoyan 2000; Blattnig et al. 2000; Mücke et al. 2003). These secondary γ -rays carry energy that is approximately one tenth of the energy of the primary protons. If CRs were accelerated up to PeV energies, we would hence expect to observe SNe and SNRs up to ultra-high energies above 100 TeV (if the sources were optically thin to photon-photon pair production at these energies). However, current TeV observations show that SNRs exhibit a softening or even a cutoff in the γ -ray spectrum before the \sim hundreds of TeV regime (e.g. Aharonian et al. 2006, 2007a,b, 2009; Abramowski et al.

★ E-mail: dimitrios.kantzas@lapth.cnrs.fr

2011; Ackermann et al. 2013; Abramowski et al. 2014; Archambault et al. 2017). Such a spectral feature questions the SN paradigm, and hence theoretical and observational investigation into new candidate sources is ongoing.

Recent TeV γ -ray observations suggest that various other Galactic sources can accelerate particles up to TeV and PeV energies. Clusters of young massive stars (Ackermann et al. 2011; Abramowski et al. 2012; Aharonian et al. 2019), pulsars (H.E.S.S. Collaboration et al. 2018b; MAGIC Collaboration et al. 2020), pulsar wind nebulae (Amenomori et al. 2019; López-Coto et al. 2022), γ -ray binaries (Aharonian et al. 2005; Hinton et al. 2008) are among the prime examples of capable sources. The latest observations of the Galactic plane from HAWC (Albert et al. 2020), LHAASO (Cao et al. 2021b) and Tibet-AS γ (Amenomori et al. 2021) found no association with SNRs and instead suggest the existence of numerous sources capable of producing γ -ray emission beyond 1 PeV with the aforementioned sources being in the list, as well as many of yet unknown nature.

The relativistic jets launched by stellar-mass black holes in X-ray binaries (BHXBs) also shine up to γ -rays. Cygnus X–3 and Cygnus X–1 (Cyg X–1) are known to emit GeV radiation (Tavani et al. 2009; Sabatini et al. 2013; Malyshev et al. 2013; Zanin et al. 2016), but it remains unclear whether the origin of this emission is due to the acceleration of electrons (Zdziarski et al. 2014) or protons (Pepe et al. 2015). There is no persistent TeV emission detected yet from these two sources (Albert et al. 2020, 2021), making it impossible to argue against or in favour of any proton acceleration in their jets. Any TeV detection however would be hard to be explained by a leptonic scenario due to Klein-Nishina suppression. The well-known case of SS433 was moreover the first BH-candidate found to emit in the TeV regime with the acceleration sites associated with the interaction of its jets with the surrounding medium (Abeysekara et al. 2018; Safi-Harb et al. 2022). More BHXBs are now detected by H.E.S.S. with the TeV emission to be along the jets (Olivera-Nieto et al. in prep).

As suggested for the case of large-scale jets of Active Galactic Nuclei (AGN), when protons accelerate to high energies above a few PeV, they also produce astrophysical neutrinos and antineutrinos via inelastic collisions that carry energy of the order of TeV-PeV (e.g. Murase et al. 2014; Petropoulou et al. 2015; Aartsen et al. 2018; Keivani et al. 2018). Astrophysical neutrinos are hence the smoking gun of CR acceleration. The current state-of-the-art neutrino detectors IceCube and ANTARES, in the South Pole and the Mediterranean Sea respectively, have not yet confirmed the Galactic origin of any neutrino to favour any particular source as a potential PeV accelerator (also known as PeVatron; Aartsen et al. 2020). The diffuse neutrino observations seem to be isotropic, implying that extragalactic sources dominate the detected spectrum at these energies (however see Kovalev et al. 2022 and De La Torre Luque et al. 2022 for a diffuse neutrino emission from the Galactic plane). The accumulated data after ten years of operation of the IceCube experiment, as well as the expected data from the next-generation facilities, such as KM3NeT/ARCA (Aiello et al. 2019) and IceCube-Gen2 (IceCube-Gen2 Collaboration et al. 2014; Aartsen et al. 2021), offer not only a unique opportunity to set new constraints on individual sources but might also start revealing Galactic and dimmer neutrino point sources.

BHXBs have been suggested as neutrino sources in the past (e.g. Levinson & Waxman 2001; Romero et al. 2003; Romero & Orellana 2005; Torres et al. 2005; Bednarek et al. 2005; Romero & Vila 2008; Reynoso et al. 2008; Zhang et al. 2010; Carulli et al. 2021; Cooper et al. 2020) but were neglected for numerous years, mainly due to the lack of γ -ray and neutrino constraints. The increasing number of newly discovered BHXBs, which may not be bright enough to be

detected in the γ -ray regime, makes the BHXB population a viable candidate to contribute to the Galactic neutrino spectrum, and hence the CR spectrum. In particular, recent X-ray observations of the Galactic centre suggest the existence of hundreds-to-thousands of BHXBs in the pc-scale of the Galactic centre (Hailey et al. 2018; Mori et al. 2021). Based on these observations, Cooper et al. (2020, hereafter C20) suggest that of the order of a few thousands of BHXBs suffice to contribute significantly to the CR spectrum, and possibly dominate the spectrum slightly above the “knee”, before the transition to the extragalactic origin.

In this work, we revisit the idea of BHXBs being Galactic CR sources and hence potential neutrino sources. We tie the multiwavelength emission of BHXB jets to the dynamical properties of the acceleration site, and hence we can derive more self-consistently predictions of the neutrino counterparts. We use, in particular, the multizone jet model of Kantzas et al. (2021, hereafter K21) that accounts for acceleration of both leptons and hadrons. The leptons accelerate to non-thermal energies to emit synchrotron radiation along the jets, being able to reproduce the flat-to-inverted radio spectra detected by multiple BHXBs (Blandford & Königl 1979; Hjellming & Johnston 1988; Falcke & Biermann 1995; Markoff et al. 2001, 2005; Lucchini et al. 2022). The accelerated protons interact inelastically with protons in the bulk flow and the jet radiation to produce secondary particles via inelastic proton-proton (pp) and proton-photon (p γ) collisions that contribute to the high-energy regime of the spectrum. We further develop this particular jet model to account for the intrinsic neutrino counterpart due to the above processes. We further investigate the contribution of BHXBs to the CR spectrum, utilising a physical jet model whose parameters we can now better constrain via the multiwavelength observations of “canonical” BHXBs, such as Cyg X–1 (K21) and GX 339–4 (Kantzas et al. 2022, hereafter K22). In particular, we use the up-to-date BHXB WATCHDOG catalogue of Tetarenko et al. (2016) to study the possibility of the intrinsic neutrino emission of these sources to contribute to the observed spectrum, and discuss the likelihood of future facilities, such as KM3NeT/ARCA, to be able to detect any Galactic neutrinos from BHXBs. We further study the contribution of these sources to the CR spectrum when the accelerated CRs escape the acceleration sites and propagate through the interstellar medium towards Earth. We finally discuss the interaction of the propagated CRs with the intergalactic medium to produce diffuse γ -rays and neutrinos.

In Section 2, we discuss the jet model we utilise to produce the intrinsic neutrino fluxes, that we present in Section 3 for the known BHXBs. In Section 4, we present our new analysis for a population of 1000 BHXBs, in Section 5 we discuss the contribution of BHXBs to the CR spectrum, and in Section 6 we summarise our results and conclude.

2 NEUTRINOS FROM BHXB JETS

Our physical jet model is based originally on work presented in Markoff et al. (2005) that explains the flat radio spectrum detected in BHXBs (see, e.g., Corbel & Fender 2002; Fender et al. 2000, 2009). In a multizone stratified jet, particles accelerate to non-thermal energies to produce the multiwavelength spectrum from radio to X-rays (Blandford & Königl 1979; Falcke & Biermann 1995; Markoff et al. 2001, 2003, 2005; Corbel et al. 2013; Russell et al. 2019; Tetarenko et al. 2021; Cao et al. 2021a). The population of primary leptons accelerates continuously along the jets beyond some specific distance (see below). The accelerated particles form a power-law distribution (in energy) and emit non-thermal synchrotron radiation that is

further upscattered to higher energies via inverse Compton scattering (Markoff et al. 2005; Lucchini et al. 2018, 2022). K21 included for the first time hadronic acceleration along the jets to account for the inelastic pp and py interactions that lead to the production of secondary electrons/positrons and γ -rays. In this work, we further self-consistently calculate the neutrino distributions that form due to the above interactions, as we describe below.

2.1 Jet dynamics and particle acceleration

Details of our multizone jet model can be found in, e.g., Markoff et al. (2005); Crumley et al. (2017); Lucchini et al. (2022) and K21, but we briefly cover the basic assumptions here for consistency. In particular, during the so-called hard X-ray spectral state, BHXBs launch bipolar, mildly relativistic and collimated jets. We assume the jets are launched at some height from the black holes, assuming a relativistically thermal lepton and cold proton composition. We do not account for any particular jet launching mechanism, as both Blandford-Znajek (Blandford & Znajek 1977) and Blandford-Payne (Blandford & Payne 1982) are viable. We assume that the leptonic population of the jet base follows a Maxwell-Jüttner distribution that is characterized by its peak temperature. The two particle distributions share the same number density, which we calculate assuming particle-number conservation along the jets. Our multi-zone jet model can account for different jet compositions including leptonic pairs (Kantzas et al. 2023), however in this work for simplicity we assume a charge neutral electron/proton jet composition throughout. Finally, we calculate the bulk velocity profile of the jets, as well as the magnetic energy density, by solving the 1D relativistic Bernoulli equation along the jet axis (Königl 1980; Crumley et al. 2017; Lucchini et al. 2022).

Whereas the particles are thermal at the jet base and remain thermal for some distance from the launching point, we assume that a fraction of them accelerates into a power law at some specific distance z_{diss} from the black hole and beyond. We assume that particles are accelerated up to some maximum energy that we calculate self-consistently by equating the acceleration timescale to the radiation loss timescales. The power-law index of the non-thermal particle distributions has been the subject of much research for decades, and it strongly depends on the nature of the acceleration site and the acceleration mechanism. Using a simple jet model we cannot capture the exact acceleration mechanism. We therefore take the power-law index p to be a free parameter. We examine in particular two different cases, first assuming a soft power-law index of $p = 2.2$, and compare it to a harder one with $p = 1.7$. We choose these two more extreme values as they could represent different acceleration mechanisms, where the soft case may favour diffusive shock acceleration (e.g. Drury 1983; Malkov & Drury 2001; Sironi & Spitkovsky 2009; Caprioli 2012; Caprioli & Spitkovsky 2014; Park et al. 2015) and the hard case magnetic reconnection in strongly magnetized plasmas (Sironi & Spitkovsky 2014; Guo et al. 2014, 2016; although also see Petropoulou & Sironi 2018 where they find evidence for a softening in the power law slope at a magnetisation ~ 50). Finally, we assume for simplicity that both electrons and protons accelerate into distributions with the same power-law index.

2.2 Lepto-Hadronic Processes

We refer the interested reader to Lucchini et al. (2022) for a detailed description of how we calculate the leptonic radiative processes; i.e., the cyclo-synchrotron emission of either thermal or non-thermal

leptons, as well as inverse Compton scattering (ICS). In this work, we describe only the hadronic processes which are responsible for the neutrino counterpart and CR acceleration.

When protons accelerate to high energy, they can interact with particles in the bulk flow and the associated radiation to initiate particle cascades that lead to the formation of secondary electrons/positrons, γ -rays and neutrinos (Rachen & Biermann 1993; Mannheim 1993; Mannheim & Schlickeiser 1994; Rachen & Mészáros 1998; Mücke et al. 2003). An alternative hadronic contribution to the electromagnetic spectrum is when accelerated protons emit synchrotron radiation (Aharonian 2002; Mücke & Protheroe 2001).

In this work, we self-consistently calculate the neutrino distributions as they emerge from the inelastic pp collisions following the semi-analytical formalism of Kelner et al. (2006). We account for both the bulk thermal protons of the flow and the cold protons of the stellar wind of the companion (K21, see Appendix E1). We use the cross-section of the pp interactions based on Kafexhiu et al. (2014):

$$\sigma_{\text{pp}}(T_p) = \left[30.7 - 0.96 \log\left(\frac{T_p}{T_{\text{thr}}}\right) + 0.18 \log^2\left(\frac{T_p}{T_{\text{thr}}}\right) \right] \times \left[1 - \left(\frac{T_{\text{thr}}}{T_p}\right)^{1.9} \right]^3 \text{ mb}, \quad (1)$$

where T_p is the proton kinetic energy in the laboratory frame and $T_{\text{thr}} = 2m_\pi + m_\pi^2/2m_p \simeq 0.2797 \text{ GeV}$ is the threshold for this interaction to take place. The formalism of Kelner et al. (2006) leads directly to steady state distributions of secondary electrons/positrons, γ -rays and neutrinos. Therefore, the underlying assumption is that intermediate unstable charged muons and pions immediately decay without radiating. This is an accurate approximation as long as the maximum energy (or Lorentz factor γ_p in fact) of the initial accelerated protons fulfils the criterion (Böttcher et al. 2013):

$$\gamma_p \ll \begin{cases} 7.8 \times 10^{11}/B \text{ for pions} \\ 5.6 \times 10^{10}/B \text{ for muons,} \end{cases} \quad (2)$$

where B is the strength of the magnetic field in the jet rest frame in units of Gauss. In the case of BHXBs where the magnetic field does not exceed the 10^5 G at the particle acceleration region, and the maximum proton energy does not go far beyond $\sim \text{PeV}$ ($\gamma_p \simeq 10^6$), we find that these two conditions are always satisfied.

The accelerated protons in the jet can also interact with the intrinsic radiation in the jet flow, and in particular with the X-ray photons emitted as synchrotron radiation of the primary electrons. We account for this inelastic py interactions that lead to the formation of secondary electrons/positrons, γ -rays and neutrinos. We follow the semi-analytical formalism of Kelner & Aharonian (2008).

In Section 5 we present the distributions of muon and electron neutrinos and anti-neutrinos from both pp and py interactions, and discuss the contribution of each distribution.

2.3 Electromagnetic spectrum

We use the broadband photon spectra computed for the canonical high-mass BHXB (HMXB) Cyg X-1 (K21), and the canonical low-mass BHXB (LMXB) GX 339-4 (Kantzas et al. 2022, hereafter K22) – see Fig. 1. Based on the jet parameters used for these spectra, we can compute self-consistently the neutrino distributions. As we discussed in the previous section, the different acceleration mechanisms may lead to different power-law indexes, so we choose to examine two different cases similar to K21 and K22. In particular, we study the case where the accelerated proton population is a soft power law

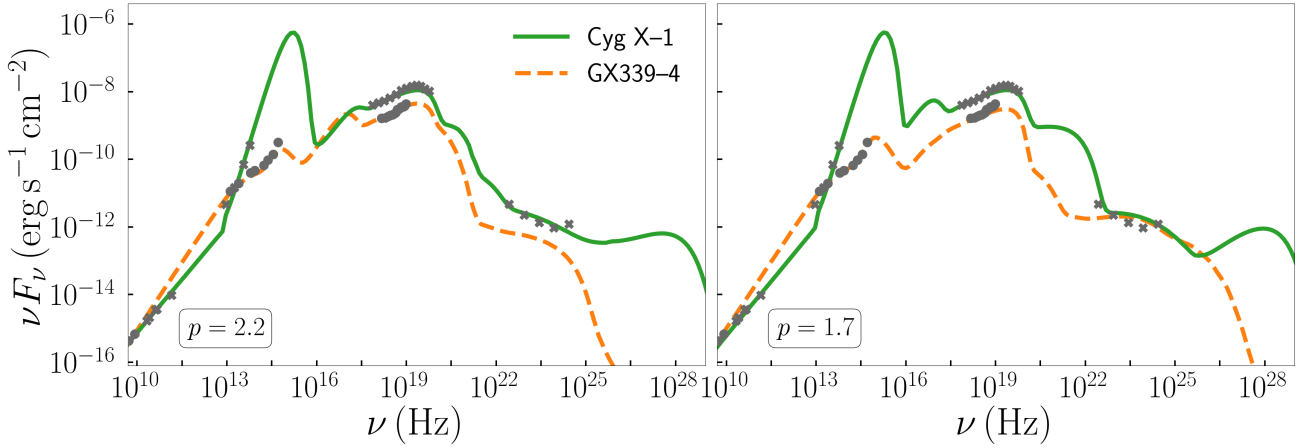


Figure 1. The predicted multiwavelength energy spectra of Cyg X–1 and GX 339–4, and the data-points we fit for (see K21 and K22, respectively, for figures with the full datasets and fits). In the *left* panel we show the soft case where the non-thermal particles accelerate in a power-law with index $p = 2.2$, and in the *right* panel we show the hard case where $p = 1.7$.

with $p = 2.2$ (left panel of Fig. 1), and compare it to a harder power law with $p = 1.7$ (right panel of Fig. 1). The former case of $p = 2.2$ explains well the flat-to-inverted radio spectrum, but recent results on modelling the spectral energy distribution of Cyg X–1 (see, e.g., Zdziarski et al. 2017; K21) suggest that a hard power law of accelerated electrons is necessary to explain the polarized emission in the MeV band as detected by *INTEGRAL* (Laurent et al. 2011; Jourdain et al. 2012; Rodriguez et al. 2015; Cangemi et al. 2021). Due to lack of similar observations on other sources, however, we examine both cases similar to K21 and K22.

3 INTRINSIC NEUTRINO EMISSION

We calculate the neutrino flux for each jet segment beyond z_{diss} for both pp and py interactions. We use in particular the formalism of Kelner et al. (2006) following equations 71 and 78 but for neutrinos instead. For the case of py interactions, we use the formalism of Kelner & Aharonian (2008) following equation 30 and the tabulated parameters of tables II and III updated by Kelner & Aharonian (2010).

3.1 Neutrino emission from Cyg X–1 and GX 339–4

In Fig. 2 we plot the integrated neutrino energy flux along the jets of Cyg X–1, for both muon neutrinos/antineutrinos (left), and electron neutrinos/antineutrinos (right). In all panels, we highlight the contribution of pp and py interactions to disentangle the contribution of each process in the GeV–PeV regime. In Appendix E1 we discuss the neutrino flux due to pp interactions for the case of Cyg X–1.

In all four panels, we see that the pp-initiated neutrinos form a power law that follows the parent power law of protons (Kelner et al. 2006), and dominates the total neutrino spectrum until tens of TeV. In particular, they share the same slope that extends to some maximum energy that is approximately one tenth of the maximum proton energy. The py neutrinos, on the other hand, form a distribution that peaks close to the maximum energy, which once again is approximately one tenth of the maximum proton energy. For the case of a hard power law of protons, the py neutrinos can dominate the high-energy regime of the spectrum, whereas for the case of a soft power law, the py neutrinos dominate in the cutoff of the spectrum.

In the upper panels of Fig. 3, we plot the electron neutrino emission

of Cyg X–1 for the two power-law slopes, $p = 1.7$ (left) and $p = 2.2$ (right), and compare it to the upper limits of the cascade-like events of IceCube after 7 yr of operation (Aartsen et al. 2019). The three different lines in both plots, correspond to the three different energy spectra as assumed by IceCube. We see that the predicted emission is below the sensitivity of IceCube by an order of magnitude, and hence the detection of any electron neutrino from Cyg X–1 is unlikely with the current generation of neutrino observatories, at least based on the typical hard state behaviour.

In the lower panels of Fig. 3, we show the total predicted electron neutrino and antineutrino emission of the jets of GX 339–4 during an outburst similar to the bright outburst in 2010. The produced neutrinos share the same properties as the parent particles. The neutrino flux of GX 339–4 is too low to be detected, which is expected based on the estimated power of the jets (K22). We also compare the predicted neutrino flux to the upper limits as set by IceCube (Aartsen et al. 2019). We see that GX 339–4 is also incapable of producing enough electron neutrinos to be detected by IceCube. In both panels, we account for neutrino oscillation such that we convert the produced rate of $\nu_\mu : \nu_e : \nu_\tau = 1 : 2 : 0$ to a detected rate at Earth $\nu_\mu : \nu_e : \nu_\tau = 1 : 1 : 1$.

3.2 Neutrino rates

The current neutrino detectors are not sensitive enough to detect a neutrino spectrum from any particular Galactic source, we can thus detect only single events. We convert the neutrino spectra to rate of events

$$R = \int 4\pi \frac{d\Phi_\nu}{dE_\nu} A_{\text{eff}}(E_\nu) dE_\nu, \quad (3)$$

where $d\Phi_\nu/dE_\nu$ is the neutrino differential flux, A_{eff} is the effective area of the detector, and we integrate between 0.1 TeV and 10 PeV. We use the effective areas of IceCube (Aartsen et al. 2013, 2019), ANTARES (Albert et al. 2017) and the simulated effective area of KM3NeT/ARCA (Adrián-Martínez et al. 2016) (see Appendix C).

In Table 1, we show the predicted event rates (per year) for the three different detectors accounting for neutrino oscillation. The number of track-like events (ν_μ and/or $\bar{\nu}_\mu$) for both IceCube and KM3NeT/ARCA is similar for the case of Cyg X–1 and around 1–1.3 neutrinos per year when the source launches jets for both $p = 2.2$ and $p = 1.7$ power-law slopes. The number of shower-like events (ν_e

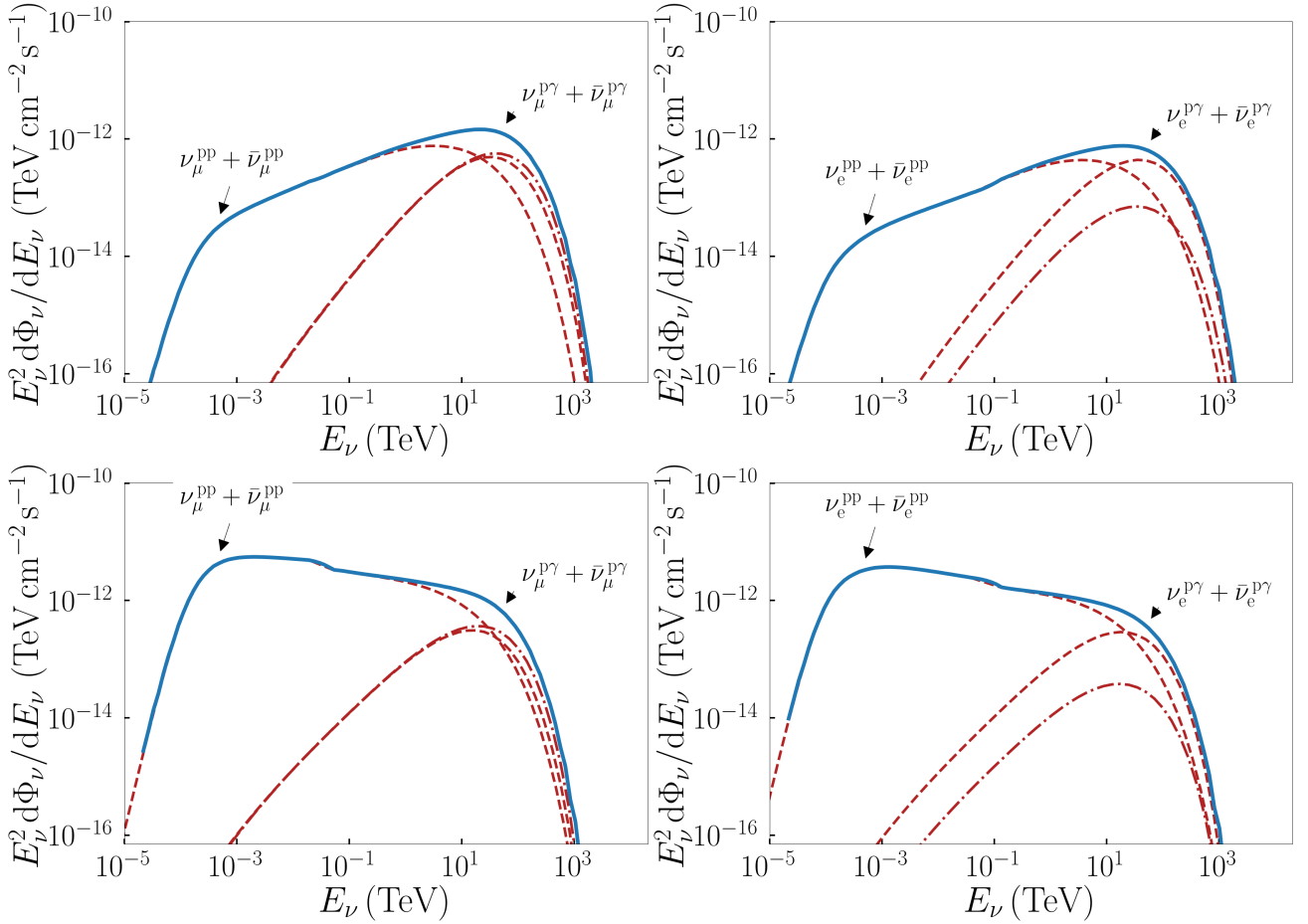


Figure 2. The intrinsic neutrino and antineutrino energy flux of the jet of Cyg X-1. In the *top* panels, the neutrinos originate in a hard power law of non-thermal protons with an index $p = 1.7$, and in the *bottom* panels, we assume $p = 2.2$. In the *left* panels, we show the distributions of muon neutrinos, and in the *right* panels, we show the electron neutrinos. The neutrinos from pp interactions always dominate the low-energy regime of the spectrum, while the neutrinos from p γ interactions dominate in the maximum energy of the order of 100 TeV. For the secondaries of p γ , we plot the muon/electron neutrinos with dashed lines, and the muon/electron antineutrino with dash-dotted lines. The solid line is for the total neutrino/antineutrino spectrum.

and/or $\bar{\nu}_e$) for IceCube is significantly reduced due to the effective area of the detector and the veto forced by the IceCube collaboration, namely the subtraction of the outer volume of the detector (Aartsen et al. 2013).

In agreement with what we expect from the neutrino energy spectrum, we see that GX 339-4 cannot produce a detectable rate of events, neither for IceCube nor KM3NeT/ARCA.

3.3 Contribution from all known BHXBs

Although we have now established that Cyg X-1 and GX 339-4 on their own cannot be detected as neutrino sources for the current generation of facilities, it is interesting to examine whether the entire population of BHXBs together would be a significant contributor to the diffuse neutrino background. We utilise the most recent XRB catalogue of Tetarenko et al. (2016) that includes all the BHXBs and BHXB-candidates detected until 2016. Out of these, we select those sources that are known BHXBs or BHXB-candidates, and known to emit in radio bands described as jet emission. This is a very conservative estimate because XRBs with neutron stars have been observed to launch jets that sometimes may be as powerful as BHXBs (see, e.g., van den Eijnden et al. 2018; Coriat et al. 2019 but also see Chatzis et al. 2021 for an alternative scenario).

From the 70 sources in the catalogue of Tetarenko et al. 2016, we consider 31 for this analysis. From these sources, 4 are HMXBs, and 27 are LMXBs. We use the neutrino spectra computed for Cyg X-1 and GX 339-4, as representative for the high-mass and LMXBs, respectively, due to the lack of better quality simultaneous observations of BHXBs. However we rescale the neutrino spectra for each source according to their distance, the mass of the black hole and the inclination. For many sources, the exact distance, the inclination and/or the mass of the black hole are not well constrained. In these cases, Tetarenko et al. (2016) assumed fiducial values: a distance of 8 kpc, the mass of the black hole equal to $8 M_{\odot}$, and an inclination angle of 60° , which we also adopt. We finally include four more LMXBs/BHXB-candidates discovered after 2016 based on the Faulkes Telescopes project (Lewis et al. 2008). We show the exact values of these sources in Table A1 of Appendix A.

In Fig. 4, we plot the differential $\nu_{\mu} + \bar{\nu}_{\mu}$ energy flux at 1 TeV for the 35 known BHXBs as a function of the declination angle δ . We compare our predicted values to the 90% median sensitivity of IceCube (Aartsen et al. 2020) and the predicted sensitivity of KM3NeT/ARCA (Aiello et al. 2019) assuming that the flux scales as E_{ν}^{-2} (solid lines) or E_{ν}^{-3} (dashed line). For simplicity, we use the publicly available sensitivity curves of IceCube with blue lines, and with a thin solid gray line the interpolated sensitivity for $p = 2.2$.

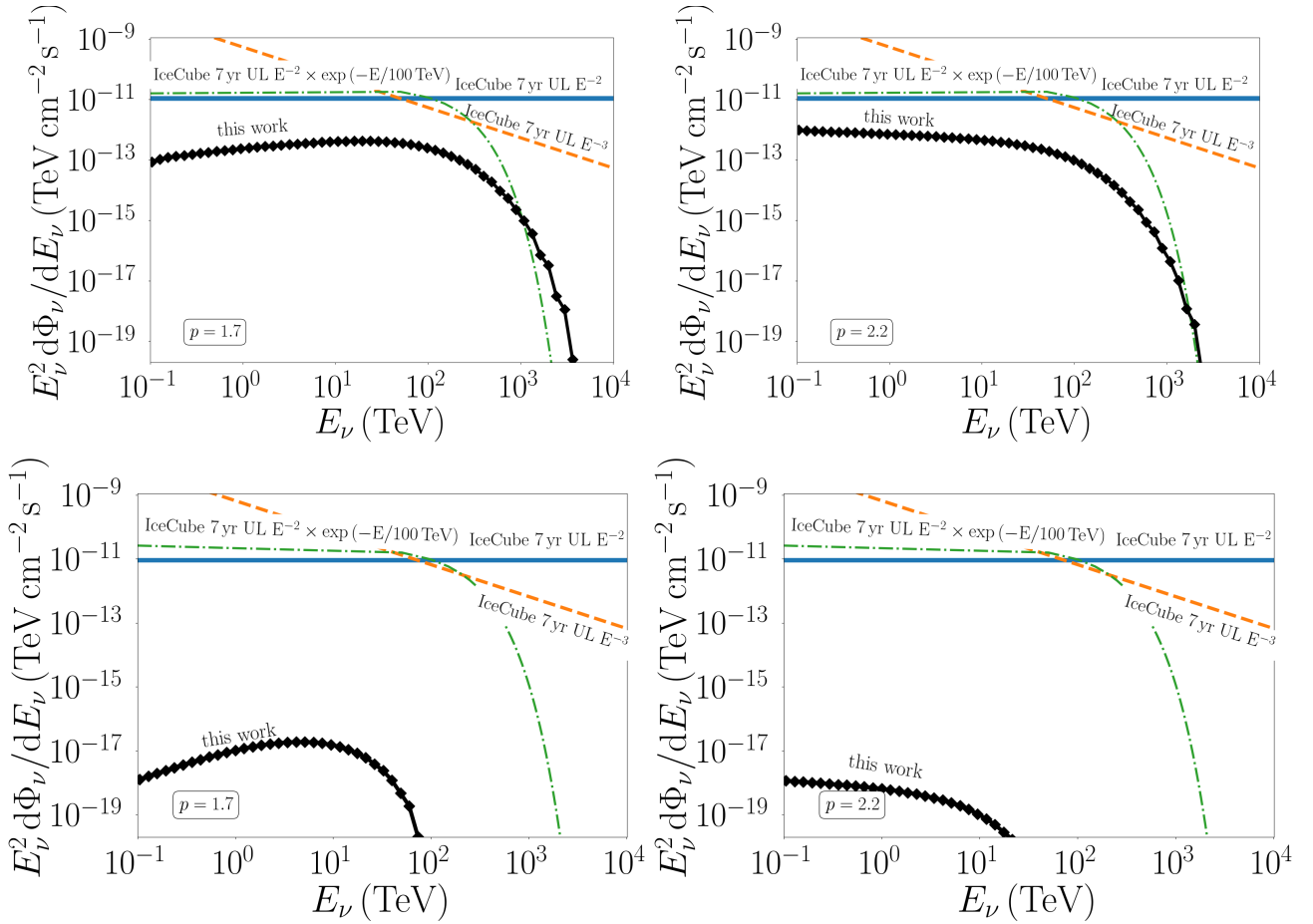


Figure 3. The total predicted $\nu_e + \bar{\nu}_e$ flux of the jets of Cyg X-1 (upper panels) and GX 339-4 (lower panels). We assume a hard power-law of accelerated protons in the *left* ($p = 1.7$) and for a soft power-law in the *right* ($p = 2.2$). We compare the predicted neutrino flux to the IceCube upper limits of cascade-like events after 7 yr of operation (Aartsen et al. 2019) for the three different assumed spectra, as indicated in the plots.

		soft proton power law ($p = 2.2$)			hard proton power law ($p = 1.7$)		
		IceCube	ANTARES	KM3NeT/ARCA	IceCube	ANTARES	KM3NeT/ARCA
Cyg X-1	$\nu_\mu + \bar{\nu}_\mu$ (yr^{-1})	1.1	0.006	1.3	1.0	0.007	1.3
	$\nu_e + \bar{\nu}_e$ (yr^{-1})	0.002	0.001	0.6	0.005	0.001	0.4
GX 339-4	$\nu_\mu + \bar{\nu}_\mu$ (yr^{-1})	7×10^{-10}	3×10^{-7}	3×10^{-5}	6×10^{-10}	3×10^{-7}	3×10^{-5}
	$\nu_e + \bar{\nu}_e$ (yr^{-1})	3×10^{-9}	3×10^{-7}	1×10^{-5}	3×10^{-9}	3×10^{-7}	1×10^{-5}

Table 1. The predicted neutrino rate (per year) for Cyg X-1 and GX 339-4 for the various detectors, and for two different proton power-law slopes. It is worth mentioning that IceCube and KM3NeT/ARCA could detect of the order of one muon neutrino from Cyg X-1 if it launched relativistic jets for a year.

Comparing to this sensitivity curve, we see that Cyg X-1 is slightly below the threshold for detection. We indicate the other HMXBs V4641 Sgr, MWC 656 and Cyg X-3 that contribute significantly to the overall predicted spectrum, as we discuss in the Appendix D. The other four LMXBs we highlight are the sources Abbasi et al. (2022) discuss in their analysis. Moreover, the LMXB with the strongest neutrino flux is MAXI J1836-194, which launches a jet with an inclination angle between 5 and 15° (Russell et al. 2014) making it a good candidate source for further spectral analysis, in particular in the case of lepto-hadronic jets (see Lucchini et al. 2021, for a purely leptonic scenario). Finally, in Fig. 4, we indicate the upper limits of those microquasars as derived by the IceCube collaboration

(Aartsen et al. 2019; Abbasi et al. 2022) for track-like events that are in the list of sources we examine in this work. The above works present multiple upper limits based on different assumptions on the energy dependence of the neutrino flux. We show only the upper limits derived under the assumption of a neutrino flux that scales as E^{-2} , because in our two models we assume a proton power-law index close to 2, and hence the produced secondaries follow a similar distribution (because the pp contribution dominates the majority of the neutrino spectrum).

In Fig. 5, we sum the intrinsic $\nu_\mu + \bar{\nu}_\mu$ emission from all 35 known BHXBs assuming either a soft power law of accelerated protons with $p = 2.2$ for every source, or a hard power law with $p = 1.7$.

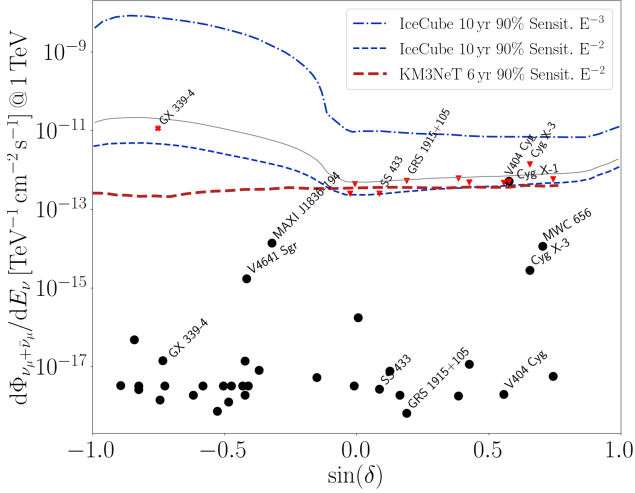


Figure 4. The predicted $\nu_\mu + \bar{\nu}_\mu$ differential flux at 1 TeV for the 35 known BHXBs we study here versus the sin of their declination (δ). We use the results for the case of $p = 2.2$. We also show the 90 per cent median sensitivity of IceCube (dot-dashed blue line for E_ν^{-3} and dashed blue line for E_ν^{-2} ; Aartsen et al. 2020) and KM3NeT/ARCA (thick, dashed red line; Aiello et al. 2019) for reference for E_ν^{-2} neutrino spectrum. We note that we cannot directly compare to these sensitivity curves because in our work we assume an $E_\nu^{-2.2}$ dependence. We hence plot the interpolated flux for $E_\nu^{-2.2}$ with a thin solid gray line. The red cross (Aartsen et al. 2019) and triangles (Abbasi et al. 2022) correspond to the 90 per cent upper limits for E_ν^{-2} .

We further assume an average duty cycle of 1 per cent (Tetarenko et al. 2016; C20; but also see Deegan et al. 2009 who suggest 0.1-0.5 per cent for the particular case of GRS 1915+105) to account for the fact that BHXBs do not launch persistent jets, but they transit between different spectral states (Belloni 2010). For the unique case of Cyg X-1 in particular, we assume a duty cycle of 25 per cent because in the past ten years, it has spent 1/4th of its time in the jet-launching state (Cangemi et al. 2021). During the so-called soft state however, the jets of HMXBs do not entirely quench but rather become less powerful, hence they may still produce neutrinos during the rest 75 per cent of their time, but at a lower rate. Comparing our results of Fig. 5 to the detected astrophysical neutrino signal of IceCube (Stettner 2019), we see that the known population of BHXBs cannot contribute more than ~ 0.2 per cent in the energy band around 40 TeV, assuming a hard proton power law. The contribution in the case of a soft power law of protons is even less than 0.1 per cent.

4 DIFFUSE SECONDARY EMISSION

4.1 BHXBs as CR sources

In the above, we calculated the intrinsic neutrino emission of 35 known BHXB jets. In this section, we use DRAGON2 (Evoli et al. 2017, 2018) to examine the contribution of a broader population of BHXBs to the CR spectrum. In particular, we conservatively assume the existence of 1000 Galactic sources that follow a spatial distribution similar to the observed distribution of pulsars (Lorimer et al. 2006), but we also account for a pc-scale spike in the number of sources close to the Galactic centre, as indicated by Mori et al.

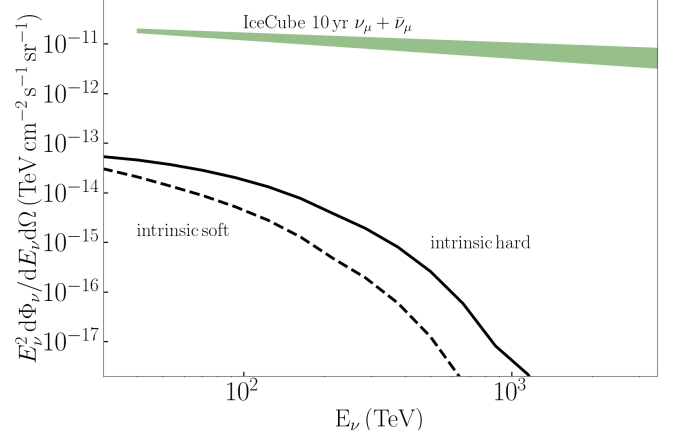


Figure 5. The predicted intrinsic $\nu_\mu + \bar{\nu}_\mu$ energy flux for the 35 known BHXBs assuming a soft power law of protons ($p = 2.2$; dashed line) or a hard power law ($p = 1.7$; solid line), assuming that the sources have a one-percent duty cycle. For comparison purposes, we also plot the astrophysical neutrino flux as observed by IceCube in 10 yr (Stettner 2019).

(2021)¹. Based on the detected BHXBs so far, we assume that 90 per cent of them are low-mass and 10 per cent are HMXBs (Tetarenko et al. 2016). Similar to our previous analysis, the BHXBs follow the behaviour of the prototypical source, therefore the jets of low BHXBs accelerate protons up to 100 TeV, and the high-mass sources accelerate protons up to 1 PeV.

Using DRAGON2, we inject CR protons which propagate in the Galactic plane in a 2D grid of radius 12 kpc and height 4 kpc. We assume in particular that the protons that escape the jets to propagate in the interstellar medium carry 10 per cent of the proton power (Blasi 2013a) and neglect any neutrons that could convert to protons (Atoyan & Dermer 2003). The results we present here scale linearly with the power carried away by the escaping particles.

In Fig. E3 we show the inverse timescales of the various cooling processes comparing them to escape. The escape rate is at least three orders of magnitudes greater than any cooling process, which means that the protons manage to escape freely, carrying the majority of their energy. The cooling processes we account are: synchrotron, pp, py, and Bethe-Heitler processes, but none of them can compare to escape, at least in the energy range we are interested in. We only propagate the population of protons as we have not included heavier elements in our previous studies to be able to further constrain their spectral properties. We adopt a spatially constant diffusion coefficient that depends on the momentum of the particle as $D = D_0(p/p_0)^\delta$, with $D_0 = 2.7 \times 10^{28} \text{ cm}^2 \text{ s}^{-1}$ and $\delta = 0.45$ (Fornieri et al. 2020; Luque et al. 2021).

In Fig. 6 we show the contribution of both LMXBs and HMXBs to the overall CR spectrum. We see that 900 LMXBs can contribute up to 50 per cent of the spectrum at the TeV energy range. The contribution falls significantly though and at ~ 100 TeV the spectrum drops exponentially (solid lines). The 100 HMXBs cannot significantly contribute to the CR spectrum even though they allow for proton energy that is 10 times greater than the one of LMXBs due to

¹ The spike of BHXBs around the Galactic centre peaks at 1 pc with a full width half maximum of 10 pc

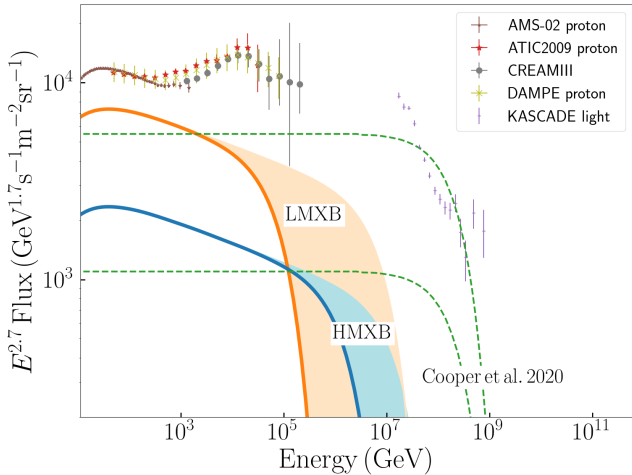


Figure 6. The contribution of a 1000 BHXBs to the CR spectrum calculated with DRAGON2. The population consists of 90 per cent LMXBs and 10 per cent of HMXBs. We assume that all the sources accelerate protons to a soft power law with an index $p = 2.2$ up to some maximum energy that depends on whether it is a low-mass or a HMXBs (solid lines). We compare our results to the observational constraints as shown in the legend, and we over-plot the “optimistic” (uppermost) and “pessimistic” (lowermost) scenarios of Cooper et al. 2020 for comparison. We show for comparison an extreme scenario (dashed lines) where the particles follow similar power-laws in energy but with larger maximum energy of the order of 10^7 GeV. The observational data are as labelled from ATIC2009 (Chang et al. 2008), CREAMIII (Yoon et al. 2017), DAMPE (DAMPE collaboration et al. 2019) and KASCADE (Apel et al. 2011).

our assumption that HMXBs are merely 10 per cent of the entire population. We moreover include the “optimistic” and the “pessimistic” scenarios of C20 for comparison, and we see that despite the similar contribution in the low-energy regime at around TeV, the approach we follow here leads to different maximum CR energy (see the discussion in Section 5.4). Finally, we overplot the shaded regions up to the extreme scenario where the maximum energy of the CRs reaches values of the order of 10^7 GeV as particle acceleration theory allows for (see Section 5.4). Such a scenario is derived from the extreme values allowed from the best fits of K21 and K22.

4.2 Diffuse gamma-ray and neutrino emission from BHXBs

After CR protons escape the acceleration site, they interact with the interstellar medium while propagating through the Galactic plane. To account for the inelastic collisions between the propagating protons and the interstellar medium, we utilise HERMES. HERMES is a publicly available code designed to compute the emission originated from a variety of non-thermal processes including synchrotron and free-free radio emission, gamma-ray emission from bremsstrahlung and inverse-Compton scattering, γ -ray and neutrino emission from pion decay (Dundovic et al. 2021). In Fig. 7, we plot the diffuse hadronic γ -rays originating from the interaction of CR protons with atomic hydrogen, the density of which is estimated from the 21 cm line emission and the molecular hydrogen indirectly traced by the CO molecular gas (Luque et al. 2022). We compare our results to the diffuse γ -ray spectrum of *Fermi*/LAT (Abdollahi et al. 2020) and the H.E.S.S. collaboration (H.E.S.S. Collaboration et al. 2018a). In

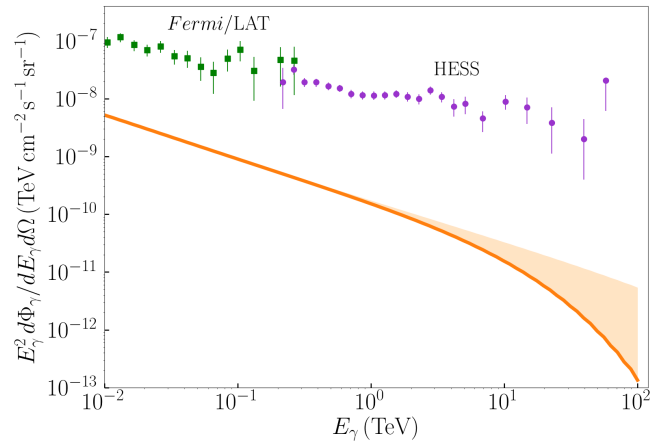


Figure 7. The diffuse γ -ray emission of CRs accelerated in BHXB jets as calculated with HERMES for Galactic latitudes within 5° from the Galactic centre. We plot the diffuse emission in the shaded region for the extreme acceleration scenario (see Fig. 6). We compare the results of *Fermi*/LAT (squares; Abdollahi et al. 2020) and the H.E.S.S. collaboration (circles; H.E.S.S. Collaboration et al. 2018a).

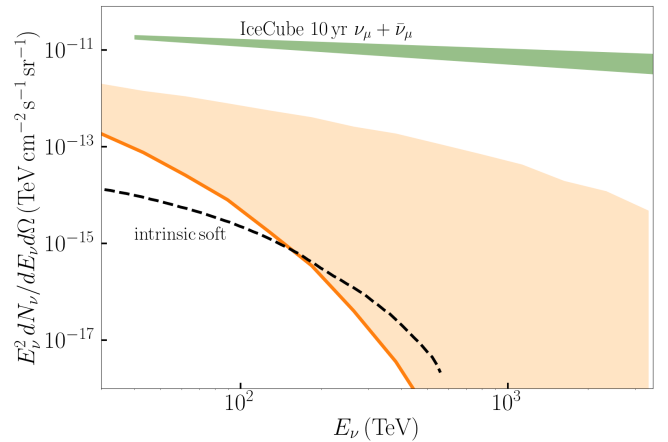


Figure 8. The diffuse neutrino emission of CRs accelerated in 1000 BHXB jets while propagating in the Galactic plane (solid line). We only account for $|b| \leq 5^{\circ}$ and $|l| \leq 180^{\circ}$, and plot the diffuse neutrino emission of IceCube for comparison (Stettner 2019). The shaded region corresponds to the diffuse neutrino emission from an extreme scenario that allows for higher proton energies (see Fig. 6), and the dashed line shows for comparison the intrinsic emission for the 35 known sources.

the aforementioned figure, we only plot the diffuse emission and do not account for the intrinsic emission of the 1000 sources because we will examine that in a forthcoming work. In Fig. 8, we plot the diffuse neutrinos of the same processes and compare them to the astrophysical background as observed by IceCube (Stettner 2019).

5 DISCUSSION

5.1 Cyg X-1 and GX 339-4 as Galactic neutrino sources

Recently, the IceCube collaboration released the updated upper limits for the Galactic BHXBs using 7.5 yr of data, where they set the 90 per cent upper limit of Cyg X-1 at $0.5 \times 10^{-12} \text{ TeV}^{-1} \text{ cm}^{-2} \text{ s}^{-1}$,

a value very close to our predicted flux (Abbasi et al. 2022). We convert the IceCube flux to fluence by multiplying with 7.5 yr to obtain $1.2 \times 10^{-4} \text{ TeV}^{-1} \text{ cm}^{-2}$. The neutrino fluence of Cyg X–1 according to our prediction is $2 \times 10^{-6} \text{ TeV}^{-1} \text{ cm}^{-2}$ assuming the neutrino production lasts for an orbital period of 6.5 days. This assumption allows us to derive the lower limit of the fluence. Despite accounting for the persistent jets Cyg X–1 launches (Rushton et al. 2012), it is difficult to identify any astrophysical neutrinos. This is in part because the TeV energy range in which we expect emission is dominated by atmospheric neutrinos (Aartsen et al. 2017a). It is also worth mentioning that Abbasi et al. (2022) assume an energy dependence of the neutrino flux with $E_\nu^{-1.25}$, which is significantly harder even compared to our hard power-law index of $p = 1.7$, inherited by the non-thermal protons. This difference in the energy dependence may relax the fact that our prediction is so close to the IceCube upper limits. In other words, if the IceCube collaboration uses a softer index, then the upper limits will increase.

In Table 1, we show the neutrino rate per year from the region of Cyg X–1. The muon neutrino rate after accounting for the effective area of IceCube and KM3NeT/ARCA are of the order of one neutrino per year, close to previous studies, such as Anchordoqui et al. 2014 where the authors used LS 5039 as a prototype. If we account for the duty cycle of Cyg X–1, the neutrino rate may decrease fourfold based on the duty cycle of Cyg X–1 the past 20 yr (Cangemi et al. 2021). Furthermore, we base our neutrino estimates on only the steady-state emission of the jets of Cyg X–1 when the system was in the inferior conjunction, such that the companion star was behind the black-hole-jet system on the line of sight. A more detailed analysis, where the orbital attenuation of the non-thermal emission is properly accounted for, is outside the scope of this work (see, e.g., Vieyro & Romero 2012, for a neutrino prediction during a flaring state). Finally, when deriving the neutrino rate from equation 3, we integrate in the energy range between 0.1 TeV and 1 PeV, thus we do not know the exact expected energy of the incoming neutrino(s). As aforementioned, the low-energy regime of the detected neutrino spectrum is dominated by the atmospheric background, therefore detectable astrophysical neutrinos from Cyg X–1 will occur in the energy range between $\sim 10 \text{ TeV}$ and $\sim 100 \text{ TeV}$.

Due to the high number of outbursts and the plethora of observations, GX 339–4 has attracted the attention of the community and several previous works have predicted the neutrino emission based on different models and/or physical processes (see, e.g., Distefano et al. 2002; Zhang et al. 2010). The muon and electron neutrino spectra we present here, and consequently the neutrino rates, are intrinsically connected to the most up-to-date multiwavelength constraints of GX 339–4 (K22). We find that GX 339–4 likely fails to be a potential source of Galactic neutrinos. The neutrinos are mainly produced in the particle acceleration region and then the flux drops along the jet. The particle acceleration region is set by the break frequency in the observed spectrum, which is variable for the case of XRBs (see e.g. Russell et al. 2014, 2019). For the case of GX 339–4 there is evidence that the synchrotron break is at $\sim 2600 R_g$, corresponding to 40000 km for a 10 solar mass black hole (Gandhi et al. 2011). This offset from the jet base is also confirmed by the 100 ms lag between X-ray and optical bands (see e.g., Kalamkar et al. 2016). In the case of Cyg X–1, on the other hand, there is no such evidence for the synchrotron break because Cyg X–1 is persistent and the cooling break is in the IR band that is dominated by the emission of the massive companion star. We hence used z_{diss} as a free parameter while fitting the multi-wavelength spectrum. The best-fit value is at $\sim 100 R_g \approx 3000 \text{ km}$ for a $21.4 M_\odot$ black hole. Moreover, the jet base radius of GX 339–4 is much larger than that of Cyg X–1 (~ 100

and $5R_g$, respectively), hence the density of the target particles is significantly decreased for the case of GX 339–4 assuming a similar injected power (of the order of $5 \times 10^{37} \text{ erg s}^{-1}$).

5.2 BHXBs as Galactic neutrino sources

Comparing the total neutrino spectrum of the 35 known BHXBs to the astrophysical background of IceCube (Stettner 2019), we find that BHXBs cannot contribute more than 0.1 percent at 40 TeV even if all the sources accelerate protons into a hard non-thermal power law with index $p = 1.7$ (see Fig. 5). The contribution of BHXBs significantly drops at larger energies and eventually cuts off at approximately 1 PeV. On the other hand, we used some very conservative assumptions and totally neglected neutron star X-ray binaries, as well as we only account for the intrinsic emission and neglect the impact the jets may have on the interstellar medium (see e.g. the case of SS 433 Abeysekara et al. 2018).

5.3 Gamma-ray emission counterpart

We compare the overall GeV-to-TeV emission of the 35 BHXB sources for the two different power-law indices to the observed flux (see Fig. 9). The H.E.S.S. collaboration has detected the Galactic plane in the same energy range, we hence use these observations for the comparison. We use the result of the best fit of the observational data that is a power-law with an exponential cutoff at 100 TeV, a photon index of $2.28 \pm 0.02_{\text{stat}} \pm 0.2_{\text{syst}}$, and a normalisation at 1 TeV of $1.2 \pm 0.04_{\text{stat}} \pm 0.2_{\text{syst}} \times 10^{-8} \text{ TeV cm}^{-2} \text{ s}^{-1} \text{ sr}^{-1}$ (H.E.S.S. Collaboration et al. 2018a). This diffuse γ -ray emission is from the inner 200 pc of the Galactic Center, but not all the sources we study here are located in this region. These observations, however, originate in a γ -ray bright region of the sky and hence we use them as an upper limit for the overall contribution of the so-far known BHXBs. We see that the predicted intrinsic high-energy emission from the BHXBs is of the order of five orders of magnitude below the H.E.S.S. observations and thus do not violate the γ -ray constraints. We stress once more though that we neglect any jet impacting on the surrounding medium that could lead to further γ -ray and neutrino emission.

5.4 BHXBs and the CR spectrum

Recent population synthesis results (see, e.g., Olejak et al. 2020), and in agreement with new X-ray observations of the Galactic centre (Hailey et al. 2018; Mori et al. 2021) suggest it is likely that of the order of 1000 accreting BHXBs exist in the Galaxy capable of launching jets. Such systems may have faint radio jets currently in quiescence, or their outbursts may otherwise be obscured. In this work, we use DRAGON2 to find their likely contribution to the CR spectrum while properly accounting for propagation in the Galactic disc (see Fig. 6). We find that BHXBs can contribute up to maximum 50 per cent in the low-energy regime of the spectrum close to TeV energies. This percentage can be decreased by a factor of 3 if the power carried away by the escaping protons is 3 per cent instead of 10 per cent of the total proton power as we assume above (Bell et al. 2013), leading to a contribution of up to ~ 17 per cent. This contribution is in broad agreement with the findings presented in C20 below the knee.

There are two notable differences between the CR contribution calculated in this work and the one in C20: the larger CR flux in the $\sim \text{TeV}$ regime of the spectrum compared to the pessimistic model of C20, and the lack of contribution at higher energies. The first can

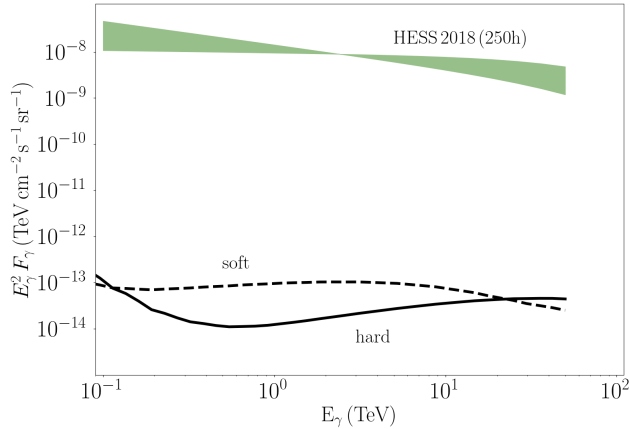


Figure 9. The overall intrinsic γ -ray emission of the 35 BHXBs of this work. We assume that the accelerated protons follow either a soft power-law of $p = 2.2$ (dashed line) or a hard power-law of $p = 1.7$ (solid line). We also plot the diffuse γ -ray emission detected after 250 hours by H.E.S.S. (H.E.S.S. Collaboration et al. 2018a) as a reference to our predicted γ -ray emission.

be explained by the fact that a softer power law is assumed, resulting in the steeper slope observed in Fig. 6. Secondly, C20 did not perform multiwavelength fitting to obtain the model parameters, but used instead some simple scaling arguments. In K21 and K22 we demonstrated that by fitting the entire spectrum we get additional constraints on the jet physical parameters that rather drastically reduce the maximum energy. Within the scope of our assumptions, we find that Cyg X-1 & GX 339-4 require a high-energy hadronic cut-off for accelerated protons at a few hundreds of TeV. Given this, we find that, at least for these prototype sources, BHXBs cannot reproduce this prominent excess in the 100 PeV energy band that would distinguish them from other Galactic or extragalactic sources, as suggested by C20. Further multi-wavelength studies of BHXBs may aid in estimating the contribution of BHXBs in the CR spectrum.

The maximum energy of accelerated CRs is an important parameter for the CR contribution, and also the neutrino spectrum. In this work, we assume that all the LMXBs follow the behaviour of the prototypical source GX 339-4 for which, based on the results of K22, protons get accelerated only up to ~ 100 TeV. In K21 and K22, we see that the maximum energy is driven by the escape and not the losses, and hence we calculate this maximum energy by equating the acceleration timescale to the confinement timescale (Hillas 1984). For a Bohm-like acceleration where particles diffusively cross a shock front (diffusive shock acceleration; DSA, also known as first-order Fermi acceleration), $t_{\text{acc}} \propto E_p / f_{sc}$, where E_p is the proton energy and f_{sc} is the ratio of the scattering mean free path to the gyroradius and is usually considered the acceleration efficiency (Jokipii 1987; Aharonian 2002). The confinement timescale $t_{\text{esc}} \propto R_{\text{acc}}$, where R_{acc} is the radius of the acceleration site. f_{sc} is the most impactful free parameter, whose exact value depends on the acceleration mechanism and is not well constrained yet. K22 set $f_{sc} = 0.01$, a value that allows for the primary electrons to reach high enough energy to radiate in the GeV regime through ICS without overshooting the Fermi/LAT upper limits (C20 assume $f_{sc} = 0.1$). Similar to K22, we assume that the acceleration efficiency is the same for both primary electrons and protons because we do not have a more robust constraint for the f_{sc} of protons. Recent numerical simulations of

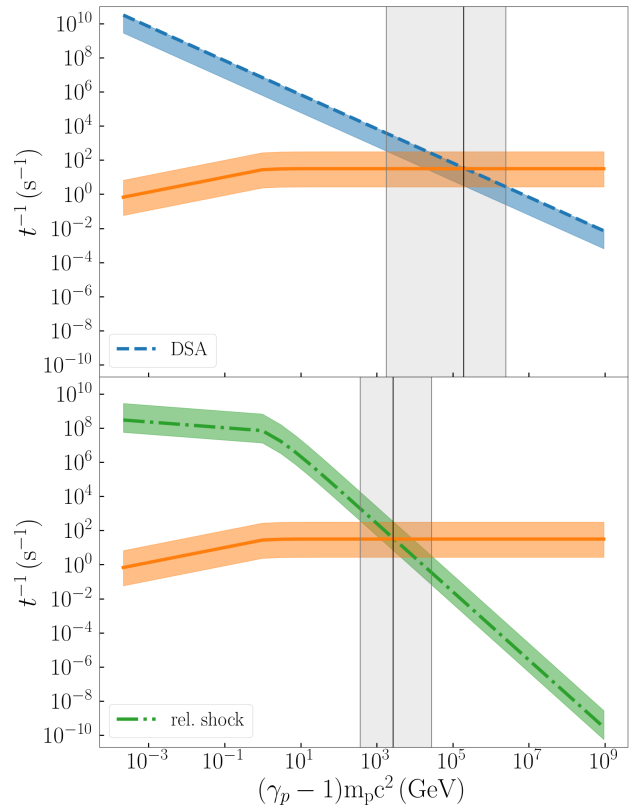


Figure 10. The acceleration and escape rates of CRs in LMXBs. When the two timescales are equal, the accelerated protons reach their maximum energy, as we show with the vertical black line. We show in both plots with a solid orange line the confinement timescale. In the *top* panel, we assume a Bohm-like, DSA-type acceleration such that $\gamma_p \propto t$ (dashed line), and in the *bottom* we assume a relativistic shock acceleration where $\gamma_p \propto t^{1/2}$ (dot-dashed line). The shaded regions show the range of the maximum energy within 1σ uncertainty.

particle acceleration though suggest that the efficiency of electrons and protons may differ, and in fact the proton acceleration may be more efficient depending on the kinematic conditions of the acceleration site (Caprioli & Spitkovsky 2014; Crumley et al. 2019). A more efficient proton acceleration would allow for protons to accelerate to energies beyond 100 TeV, and hence allowing for the BHXB population to contribute more significantly in the CR spectrum, as in C20.

The efficiency of the particle acceleration also depends on the magnetisation of the shock and its medium, as well as the obliquity of the system, which is defined as the angle between the upstream magnetic field vector and the shock normal. In relativistic, magnetised media as we expect in the jets we examine here, when the magnetic field is almost aligned with the shock front, DSA is thought to be inefficient (Sironi et al. 2013). In that case in particular, the acceleration timescale based on particle-in-cell numerical simulations (PIC) is $t_{\text{acc,pic}} = 4\gamma_p^2 / \Gamma^2 \omega_{pi}$ (Sironi et al. 2013). Here, $\omega_{pi} = \sqrt{m_e/m_p} \omega_{pe}$ and $\omega_{pe} = (4\pi e^2 n_e / \Gamma m_e)^{1/2}$ are the plasma

frequencies for the protons and the electrons, respectively. In the plasma frequency, e is the elementary charge, n_e is the number density of the particles at the acceleration region, and Γ is its bulk Lorentz factor.

In Fig. 10, we plot the acceleration and escape rates as a function of the proton energy $(\gamma_p - 1)m_p c^2$. The intersection of the two lines, indicates the maximum energy that protons can attain. In the top panel, we use the Bohm acceleration timescale, and in the bottom, we use the relativistic shock acceleration according to Sironi et al. (2013) with $n_e = 10^{11} \text{ cm}^{-3}$ and $\Gamma = 2$. In both panels of Fig. 10, we show the exact timescales (solid line for escape, dashed line for Bohm acceleration, dot-dashed line for relativistic shock) and indicate the maximum energy with a black vertical line. We show the possible values of the maximum energy within the shaded regions that are within the 1σ uncertainty of the free parameters (see Table 3 of K22) and for $0.001 \leq f_{sc} \leq 0.1$, where the former boundary indicates a relatively inefficient acceleration and the latter indicates an efficient particle acceleration. The exact dynamical values we use here correspond to the first particle acceleration region of the jet, but beyond that region, the maximum energy remains almost constant (see Fig. 4 of C20). Overall, we see that protons in BHXBs can in principle accelerate to a maximum energy that ranges between 400 GeV and 2.5 PeV.

An alternative plausible acceleration mechanism which could be more efficient, is magnetic reconnection (Drenkhahn & Spruit 2002; Uzdensky 2011; Guo et al. 2014; Sironi & Spitkovsky 2014; Sironi et al. 2015; Kagan et al. 2015). The acceleration timescale of magnetic reconnection scales as $t_{\text{rec}} \propto E_p$ and based on PIC simulations, $t_{\text{rec}} = E_p / (0.1ecB)$, where the factor 0.1 comes from the reconnection rate of the field lines $r_{\text{rec}} = v_{\text{in}}/v_A$ (Sironi & Spitkovsky 2014). In the case of a strongly magnetised medium, the Alfvén velocity $v_A = c\sqrt{\sigma/(1+\sigma)} \approx c$, and hence the inflow velocity $v_{\text{in}} \approx 0.1c$. The inflow velocity defines the electric field responsible for the acceleration $E_{\text{rec}} \approx 0.1B$ (Uzdensky 2011; Sironi & Spitkovsky 2014). Comparing the reconnection timescale to the Bohm acceleration timescale, we see that for $f_{sc} \approx 0.1$, the two timescales are equal if Bohm acceleration is very efficient. In strong magnetised regions, however, one has to consider the effect of the synchrotron radiation on the accelerated particles, and hence a more self-consistent treatment is necessary (Hakobyan et al. 2019; Ripperda et al. 2022). Consequently, in the efficient acceleration regime of DSA, or in the case of magnetic reconnection where particles do not radiate away their energy immediately, it is likely for LMXB jets to accelerate particles to slightly larger energies. If such a scenario is feasible for the majority of the Galactic LMXBs, then that would increase their contribution to the CR spectrum (Fig. 6). In Fig. E4 we show the maximum CR energy for the case of HMXBs based on K21.

5.5 Heavier element contribution

The non-thermal acceleration of heavier nuclei in shocks is more efficient because the acceleration timescale scales inversely with the charge of the accelerated element (see e.g. Caprioli et al. 2011, for the case of SNRs). However, there is no evidence for non-thermal acceleration of heavier elements in ‘normal’ BHXBs. There is only the case of SS433 that shows iron line emission (Migliari et al. 2002) but this is a unique system embedded in a nebula and seemingly quite slow mass loaded. To properly account for heavier elements in our approach, we require the exact abundances that based on the Galactic CR proton-to-helium ratio is less than 10 per cent for energies above $\sim 10\text{GeV}$ (Adriani et al. 2011), and the proton-to-iron ratio drops way below 10 per cent for CR energies below 1TeV (Thoudam, S. et al.

2016). Moreover, to calculate the products of inelastic interactions of heavier elements, we need the cross-sections that are less constrained than proton cross-sections. Hence, the assumption of only protons is fair within the astrophysical uncertainties.

6 SUMMARY AND CONCLUSIONS

Despite detailed studies over many decades, we still do not fully understand the origin of CRs, even those of Galactic nature. CRs are deflected after leaving their acceleration sites due to the Galactic magnetic field, making it impossible to use their location on the sky to pinpoint their sources. We can however use indirect, multi-messenger means to examine the CR acceleration in astrophysical sources by studying the intrinsic γ -rays and neutrinos produced, as well as the diffuse emission when accelerated CRs interact with the surrounding medium and/or radiation.

In this work, we have presented a multizone, lepto-hadronic model for BHXB jets (in the hard state), which accounts for neutrino distributions due to the inelastic pp and py collisions (Kelner et al. 2006 and Kelner & Aharonian 2008, respectively). We first produce the intrinsic neutrino distributions for the two canonical BHXBs, namely the high-mass Cyg X–1, and the low-mass GX 339–4. We constrain the neutrino emission based on the work of K21 for Cyg X–1 and K22 for GX 339–4, who constrain the proton acceleration in the BHXB jets by reproducing the multiwavelength radio-to- γ -ray spectrum. We expand our predictions on the intrinsic neutrino emission for 35 known BHXBs discovered so far. We find that Cyg X–1 is a promising candidate neutrino source (~ 1 muon neutrino per year while in hard state for IceCube), and in fact, our predicted muon neutrino flux is close to the most up-to-date upper-limits set by IceCube. From the other 34 sources, only one more source (MAXI J1836-194) might warrant further, more detailed investigation.

Future imaging Cherenkov telescopes, such as the Cherenkov Telescope Array (Acharya et al. 2013) will be up to five orders of magnitude more sensitive to transient BHXB jet outburst than current facilities. Cubic kilometer neutrino detectors, such as KM3NeT/ARCA (Adrián-Martínez et al. 2016) in the Mediterranean Sea, Baikal Deep Underwater Neutrino Telescope in Baikal (and RALF WISCHNEWSKI et al. 2005) and IceCube-Gen2 in the South Pole, which will be 5 times more sensitive than the current facilities (IceCube-Gen2 Collaboration et al. 2014; Aartsen et al. 2021), will be able to further constrain the diffuse emission, and hence lead to a better understanding of CR acceleration.

Recent X-ray observations of the Galactic centre support the existence of hundreds to thousands BHXBs in quiescence that remain undetected due to their duty cycle. In this work, we assume the existence of 1000 such sources distributed in the Galaxy capable of accelerating CRs following the behaviour of the two prototypical sources in the hard state. When CRs escape the acceleration sites, they interact with the Galactic molecular gas while they propagate in the Galactic plane, to produce further γ -rays and neutrinos that contribute to the diffuse spectra we detect on Earth. To properly study the CR propagation we use DRAGON2 (Evoli et al. 2017, 2018), and to self-consistently calculate the γ -ray and neutrino counterparts, we use the publicly available code HERMES (Dundovic et al. 2021). These 1000 BHXBs are able to contribute up to 50 per cent in the TeV regime of the CR spectrum, but whether they can contribute in the PeV regime strongly depends on the particle acceleration properties that are still poorly constrained. This contribution of 50 per cent in the TeV regime would decrease if the power of protons that escape the jets is less than 10 per cent of the total proton power as we assumed

in this work. Finally, the exact number of the Galactic BHXBs is not well constrained but according to the early data release of the third *Gaia* catalogue ([Gaia Collaboration et al. 2021](#); [Gomel et al. 2022](#)), which includes over 30 million stars, *Gaia* will be able to classify non-single stars and provide a more accurate number of BHXBs in quiescence, which are all candidate CR sources when they go into outbursts. If these sources can also contribute to the non-thermal γ -ray and neutrino emission, remains an open question that can we can tackle with the development of better theoretical infrastructure similar to this work.

The field of high-energy astrophysics with Galactic transient sources, especially those that launch relativistic jets, is in rapid development. Now that we know that the jets of several BHXBs interact with the surrounding medium leading to hundreds of TeV γ -rays ([Abeyssekara et al. 2018](#), [Olivera-Nieto et al. in prep](#)) we may need to add another location for particle acceleration in the interstellar medium that would have different conditions but also implications on our understanding of CR sources.

ACKNOWLEDGEMENTS

We would like to thank the anonymous reviewer for their fruitful comments to improve the quality of the manuscript. DK acknowledges funding from the French Programme d'investissements d'avenir through the Enigmass Labex. SM and DK are grateful for support from the Dutch Research Council (NWO) VICI grant (no. 639.043.513). PTL is supported by the Swedish Research Council under contract 2019-05135. DG acknowledges support from the project "Theoretical Astroparticle Physics (TASP)" funded by the INFN.

DATA AVAILABILITY

No new data were generated or analysed in support of this research.

REFERENCES

Aartsen M. G., et al., 2013, *Science*, **342**, 1242856
Aartsen M. G., et al., 2015, *ApJ*, **809**, 98
Aartsen M. G., et al., 2016, *ApJ*, **833**, 3
Aartsen M. G., et al., 2017a, *ApJ*, **835**, 151
Aartsen M. G., et al., 2017b, *ApJ*, **849**, 67
Aartsen M., et al., 2018, *Science*, **361**, 1378
Aartsen M. G., et al., 2019, *ApJ*, **886**, 12
Aartsen M. G., et al., 2020, *Phys. Rev. Lett.*, **124**, 051103
Aartsen M. G., et al., 2021, *J. Phys. G: Nucl. Part. Phys.*, **48**, 060501
Abbasi R., et al., 2022, *ApJ Letters*, **930**, L24
Abdo A., et al., 2008, *ApJ*, **688**
Abdollahi S., et al., 2020, *ApJ Supplement Series*, **247**, 33
Abeyssekara A., et al., 2018, *Nature*, **562**, 82
Abramowski A., et al., 2011, *A&A*, **531**, A81
Abramowski A., et al., 2012, *A&A*, **537**, A114
Abramowski A., et al., 2014, *MNRAS*, **439**, 2828
Abramowski A., et al., 2016, *Nature*, **531**, 476
Abreu P., et al., 2021, *The European Physical Journal C*, **81**
Acharya B., et al., 2013, *Astroparticle Physics*, **43**, 3
Ackermann M., et al., 2011, *Science*, **334**, 1103
Ackermann M., et al., 2012, *ApJ*, **750**, 3
Ackermann M., et al., 2013, *Science*, **339**, 807
Adrián-Martínez S., et al., 2016, *J. Phys. G: Nucl. Part. Phys.*, **43**, 084001
Adriani O., et al., 2011, *Science*, **332**, 69
Adrián-Martínez S., et al., 2016, *Physics Letters B*, **760**, 143
Aharonian F., 2002, *MNRAS*, **332**, 215

Aharonian F. A., Atayan A. M., 2000, [arXiv:0009009](#)
Aharonian F., et al., 2005, *Science*, **309**, 746
Aharonian F., et al., 2006, *A&A*, **449**, 223
Aharonian F., et al., 2007a, *A&A*, **464**, 235
Aharonian F., et al., 2007b, *ApJ*, **661**, 236
Aharonian F., et al., 2009, *ApJ*, **692**, 1500
Aharonian F., Yang R., de Oña Wilhelmi E., 2019, *Nature Astronomy*, **3**, 561
Aiello S., et al., 2019, *Astroparticle Physics*, **111**, 100
Albert A., et al., 2017, *Phys. Rev. D*, **96**, 082001
Albert A., et al., 2018, *ApJ*, **868**, L20
Albert A., et al., 2020, *ApJ*, **905**, 76
Albert A., et al., 2021, *ApJ Letters*, **912**, L4
Aleksić J., et al., 2015, *A&A*, **576**, A36
Amenomori M., et al., 2019, *Phys. Rev. Lett.*, **123**, 051101
Amenomori M., et al., 2021, *Phys. Rev. Lett.*, **126**, 141101
Anchordoqui L. A., Goldberg H., Paul T. C., da Silva L. H. M., Vlcek B. J., 2014, *Phys. Rev. D*, **90**, 123010
Apel W. D., et al., 2011, *Phys. Rev. Lett.*, **107**, 171104
Archambault S., et al., 2017, *ApJ*, **836**, 23
Atayan A. M., Dermer C. D., 2003, *ApJ*, **586**, 79
Atri P., et al., 2020, *MNRAS: Letters*, **493**, L81
Baade W., Zwicky F., 1934, *Proceedings of the National Academy of Sciences*, **20**, 259
Bednarek W., Burgio G., Montaruli T., 2005, *New Astronomy Reviews*, **49**, 1
Bell A. R., Schure K. M., Reville B., Giacinti G., 2013, *Monthly Notices of the Royal Astronomical Society*, **431**, 415
Belloni T., ed. 2010, *The Jet Paradigm Lecture Notes in Physics*, Berlin Springer Verlag Vol. 794, [doi:10.1007/978-3-540-76937-8](#).
Belloni T. M., Zhang L., Kylafis N. D., Reig P., Altamirano D., 2020, *MNRAS*, **496**, 4366
Berezinsky V., 1991, *Nucl. Phys. B Proc. Suppl.*, **19**, 375
Blandford R., Königl A., 1979, *ApJ*, **232**, 34
Blandford R. D., Payne D. G., 1982, *MNRAS*, **199**, 883
Blandford R. D., Znajek R. L., 1977, *MNRAS*, **179**, 433
Blasi P., 2013a, *The A&A Review*, **21**, 70
Blasi P., 2013b, *Nuclear Physics B Proceedings Supplements*, **239**, 140
Blattinig S. R., Swaminathan S. R., Kruger A. T., Ngom M., Norbury J. W., 2000, *Phys. Rev. D*, **62**, 094030
Böttcher M., Reimer A., Sweeney K., Prakash A., 2013, *ApJ*, **768**, 54
Buitink S., et al., 2016, *Nature*, **531**, 70
Cangemi F., et al., 2021, *A&A*, **650**, A93
Cao Z., Lucchini M., Markoff S., Connors R. M. T., Grinberg V., 2021a, *MNRAS*, **509**, 2517
Cao Z., Aharonian F. A., An Q., Axikegu Bai L. X., Bai Y. X., Bao Y. W., Bastieri D., 2021b, *Nature*, **594**, 33
Caprioli D., 2012, *J. Cosmology Astropart. Phys.*, 2012, 038
Caprioli D., Spitkovsky A., 2014, *ApJ*, **783**, 91
Caprioli D., Blasi P., Amato E., 2011, *Astroparticle Physics*, **34**, 447
Carulli A. M., Reynoso M. M., Romero G. E., 2021, *Astroparticle Physics*, **128**, 102557
Chang J., et al., 2008, *Nature*, **456**, 362
Chatzis M., Petropoulou M., Vasilopoulos G., 2021, *MNRAS*, **509**, 2532
Chauhan J., et al., 2019, *MNRAS: Letters*, **488**, L129
Cooper A. J., Gaggero D., Markoff S., Zhang S., 2020, *MNRAS*, **493**, 3212
Corbel S., Fender R. P., 2002, *ApJ*, **573**, L35
Corbel S., et al., 2013, *MNRAS: Letters*, **431**, L107
Coriat M., Fender R. P., Tasse C., Smirnov O., Tzioumis A. K., Broderick J. W., 2019, *MNRAS*, **484**, 1672
Crumley P., Ceccobello C., Connors R. M. T., Cavecchi Y., 2017, *A&A*, **601**, A87
Crumley P., Caprioli D., Markoff S., Spitkovsky A., 2019, *MNRAS*, **485**, 5105
DAMPE collaboration et al., 2019, *Science advances*, **5**, eaax3793
De La Torre Luque P., Gaggero D., Grasso D., Marinelli A., 2022, *Frontiers in Astronomy and Space Sciences*, **9**
Deegan P., Combet C., Wynn G. A., 2009, *MNRAS*, **400**, 1337
Dermer C. D., 1986, *A&A*, **157**, 223

- Distefano C., Guetta D., Waxman E., Levinson A., 2002, *ApJ*, **575**, 378
- Drenkhahn G., Spruit H. C., 2002, *A&A*, **391**, 1141
- Drury L. O., 1983, *Rep. Prog. Phys.*, **46**, 973
- Dundovic A., Evoli C., Gaggero D., Grasso D., 2021, *A&A*, **653**, A18
- Evoli C., Gaggero D., Vittino A., Bernardo G. D., Mauro M. D., Ligorini A., Ullio P., Grasso D., 2017, *J. Cosmology Astropart. Phys.*, **2017**, 015
- Evoli C., Gaggero D., Vittino A., Mauro M. D., Grasso D., Mazziotta M. N., 2018, *J. Cosmology Astropart. Phys.*, **2018**, 006
- Falcke H., Biermann P. L., 1995, *A&A*, **293**, 665
- Fender R. P., Pooley G. G., Durouchoux P., Tilanus R. P. J., Brocksopp C., 2000, *MNRAS*, **312**, 853
- Fender R. P., Homan J., Belloni T. M., 2009, *MNRAS*, **396**, 1370
- Feyereisen M. R., Tamborra I., Ando S., 2017, *J. Cosmology Astropart. Phys.*, **2017**, 057
- Fornieri O., Gaggero D., Grasso D., 2020, *JCAP*, **2020**, 009
- Gaggero D., Grasso D., Marinelli A., Urbano A., Valli M., 2015, *ApJ*, **815**, L25
- Gaia Collaboration et al., 2021, *A&A*, **649**, A1
- Gaissler T. K., Engel R., Resconi E., 2016, *Cosmic rays and particle physics*. Cambridge University Press, doi:10.1017/CBO9781139192194
- Gandhi P., et al., 2011, *ApJ*, **740**, L13
- Ginzburg V. L., Syrovatskii S. I., 1964, *The Origin of Cosmic Rays*. Elsevier
- Gomel R., et al., 2022, arXiv:2206.06032,
- Guo F., Li H., Daughton W., Liu Y.-H., 2014, *Phys. Rev. Lett.*, **113**, 155005
- Guo F., et al., 2016, *ApJ*, **818**, L9
- H.E.S.S. Collaboration et al., 2018a, *A&A*, **612**, A9
- H.E.S.S. Collaboration et al., 2018b, *A&A*, **620**, A66
- Hailey C. J., Mori K., Bauer F. E., Berkowitz M. E., Hong J., Hord B. J., 2018, *Nature*, **556**, 70
- Hakobyan H., Philippov A., Spitkovsky A., 2019, *ApJ*, **877**, 53
- Hillas A. M., 1984, *Annual review of A&A*, **22**, 425
- Hinton J. A., et al., 2008, *ApJ*, **690**, L101
- Hjellming R., Johnston K., 1988, *ApJ*, **328**, 600
- IceCube-Gen2 Collaboration et al., 2014, arXiv:1412.5106
- Jokipii J., 1987, *ApJ*, **313**, 842
- Jourdain E., Roques J., Chauvin M., Clark D., 2012, *ApJ*, **761**, 27
- Kafexhiu E., Aharonian F., Taylor A., Vila G., 2014, *Physical Review D*, **90**, 123014
- Kagan D., Sironi L., Cerutti B., Giannios D., 2015, *Space-Sci.-Rev.*, **191**, 545
- Kalamkar M., Casella P., Uttley P., O'Brien K., Russell D., Maccarone T., van der Klis M., Vincentelli F., 2016, *MNRAS*, **460**, 3284
- Kantzas D., et al., 2021, *MNRAS*, **500**, 2112
- Kantzas D., Markoff S., Lucchini M., Ceccobello C., Grinberg V., Connors R. M. T., Uttley P., 2022, *MNRAS*, **510**, 5187
- Kantzas D., Markoff S., Lucchini M., Ceccobello C., Chatterjee K., 2023, *MNRAS*, **520**, 6017
- Keivani A., et al., 2018, *ApJ*, **864**, 84
- Kelner S., Aharonian F., 2008, *Physical Review D*, **78**, 034013
- Kelner S. R., Aharonian F. A., 2010, *Phys. Rev. D*, **82**, 099901
- Kelner S., Aharonian F. A., Bugayov V., 2006, *Physical Review D*, **74**, 034018
- Königl A., 1980, *The Physics of Fluids*, **23**, 1083
- Kovalev Y. Y., Plavin A. V., Troitsky S. V., 2022, *APJ Letters*, **940**, L41
- Laurent P., Rodriguez J., Wilms J., Cadolle Bel M., Pottschmidt K., Grinberg V., 2011, *Science*, **332**, 438
- Levinson A., Waxman E., 2001, *Phys. Rev. Lett.*, **87**, 171101
- Lewis F., Russell D. M., Fender R. P., Roche P., Clark J. S., 2008, arXiv:0811.2336
- López-Coto R., de Oña Wilhelmi E., Aharonian F., Amato E., Hinton J., 2022, *Nature Astronomy*, pp 1–8
- Lorimer D. R., et al., 2006, *MNRAS*, **372**, 777
- Lucchini M., Markoff S., Crumley P., Krauß F., Connors R. M. T., 2018, *MNRAS*, **482**, 4798
- Lucchini M., Russell T. D., Markoff S. B., Vincentelli F., Gardenier D., Ceccobello C., Uttley P., 2021, *MNRAS*, **501**, 5910
- Lucchini M., et al., 2022, *MNRAS*, **517**, 5853
- Luque P. D. L. T., Mazziotta M., Loparco F., Gargano F., Serini D., 2021, *JCAP*, **2021**, 010
- Luque P. D. L. T., Gaggero D., Grasso D., Fornieri O., Egberts K., Steppa C., Evoli C., 2022, arXiv:2203.15759
- MAGIC Collaboration et al., 2020, *A&A*, **643**, L14
- Malkov M., Drury L. O., 2001, *Rep. Prog. Phys.*, **64**, 429
- Malyshev D., Zdziarski A. A., Chernyakova M., 2013, *MNRAS*, **434**, 2380
- Mannheim K., 1993, *A&A*, **269**, 67
- Mannheim K., Schlickeiser R., 1994, *A&A*, **286**, 983
- Markoff S., Falcke H., Fender R., 2001, *A&A*, **372**, L25
- Markoff S., Nowak M., Corbel S., Fender R., Falcke H., 2003, *A&A*, **397**, 645
- Markoff S., Nowak M. A., Wilms J., 2005, *ApJ*, **635**, 1203
- Migliari S., Fender R., Méndez M., 2002, *Science*, **297**, 1673
- Miller-Jones J. C. A., et al., 2021, *Science*, **371**, 1046
- Mori K., et al., 2021, *ApJ*, **921**, 148
- Mücke A., Protheroe R., 2001, *Astroparticle Physics*, **15**, 121
- Mücke A., Protheroe R., Engel R., Rachen J., Stanev T., 2003, *Astroparticle Physics*, **18**, 593
- Murase K., Inoue Y., Dermer C. D., 2014, *Phys. Rev. D*, **90**, 023007
- Oda S., et al., 2019, *PASJ*, **71**, 108
- Olejak A., Belczynski K., Bulik T., Sobolewska M., 2020, *A&A*, **638**, A94
- Orosz J. A., et al., 2001, *ApJ*, **555**, 489
- Park J., Caprioli D., Spitkovsky A., 2015, *Phys. Rev. Lett.*, **114**, 085003
- Pepe C., Vila G. S., Romero G. E., 2015, *A&A*, **584**, A95
- Petropoulou M., Sironi L., 2018, *MNRAS*, **481**, 5687
- Petropoulou M., Dimitrakoudis S., Padovani P., Mastichiadis A., Resconi E., 2015, *MNRAS*, **448**, 2412
- Pierre-Auger C., 2023, *Journal of Physics: Conference Series*, **2429**, 012009
- Prodanović T., Fields B. D., Beacom J. F., 2007, *Astroparticle Physics*, **27**, 10
- Rachen J. P., Biermann P. L., 1993, *A&A*, **272**, 161
- Rachen J. P., Mészáros P., 1998, *Phys. Rev. D*, **58**, 123005
- Reynoso M. M., Romero G. E., Christiansen H. R., 2008, *MNRAS*, **387**, 1745
- Ripperda B., Liska M., Chatterjee K., Musoke G., Philippov A. A., Markoff S. B., Tchekhovskoy A., Younsi Z., 2022, *ApJ Letters*, **924**, L32
- Rodriguez J., et al., 2015, *ApJ*, **807**, 17
- Romero G. E., Orellana M., 2005, *A&A*, **439**, 237
- Romero G. E., Vila G. S., 2008, *A&A*, **485**, 623
- Romero G. E., Torres D. F., Bernadó M. K., Mirabel I., 2003, *A&A*, **410**, L1
- Rushton A., et al., 2012, *MNRAS*, **419**, 3194
- Russell T. D., Soria R., Motch C., Pakull M. W., Torres M. A. P., Curran P. A., Jonker P. G., Miller-Jones J. C. A., 2014, *MNRAS*, **439**, 1381
- Russell T. D., et al., 2019, *ApJ*, **883**, 198
- Sabatini S., et al., 2013, *ApJ*, **766**, 83
- Safi-Harb S., et al., 2022, *The Astrophysical Journal*, **935**, 163
- Schneider A., 2019, arXiv:1907.11266
- Sironi L., Spitkovsky A., 2009, *ApJ*, **698**, 1523
- Sironi L., Spitkovsky A., 2014, *ApJ*, **783**, L21
- Sironi L., Spitkovsky A., Arons J., 2013, *ApJ*, **771**, 54
- Sironi L., Petropoulou M., Giannios D., 2015, *MNRAS*, **450**, 183
- Stephens S., Badhwar G., 1981, *Astrophysics and Space Science*, **76**, 213
- Stettner J., 2019, arXiv:1908.09551
- TA C., 2022, Highlights from the Telescope Array Experiments, doi:10.48550/ARXIV.2209.03591
- Tavani M., et al., 2009, *Nature*, **462**, 620
- Tetarenko B. E., Sivakoff G. R., Heinke C. O., Gladstone J. C., 2016, *ApJ Supplement Series*, **222**, 15
- Tetarenko A. J., et al., 2021, *MNRAS*, **504**, 3862
- Thoudam, S. Rachen, J. P. van Vliet, A. Achterberg, A. Buitink, S. Falcke, H. Hörandel, J. R. 2016, *A&A*, **595**, A33
- Torres D. F., Romero G. E., Mirabel F., 2005, *Chinese Astron. Astrophys.*, **5**, 183
- Uzdensky D. A., 2011, *Space Sci. Rev.*, **160**, 45
- Vieyro F. L., Romero G. E., 2012, *A&A*, **542**, A7
- Yoon Y. S., et al., 2017, *ApJ*, **839**, 5
- Zanin R., Fernández-Barral A., de Oña Wilhelmi E., Aharonian F., Blanch O., Bosch-Ramon V., Galindo D., 2016, *A&A*, **596**, A55
- Zdziarski A. A., Pjanka P., Sikora M., Stawarz L., 2014, *MNRAS*, **442**, 3243

Zdziarski A. A., Malyshev D., Chernyakova M., Pooley G. G., 2017, *MNRAS*, **471**, 3657
 Zhang J. F., Feng Y. G., Lei M. C., Tang Y. Y., Tian Y. P., 2010, *MNRAS*, **407**, 2468
 and RALF WISCHNEWSKI et al., 2005, *International Journal of Modern Physics A*, **20**, 6932
 van den Eijnden J., Degenaar N., Russell T., Wijnands R., Miller-Jones J., Sivakoff G., Hernández Santisteban J., 2018, *Nature*, **562**, 233

APPENDIX A: DETECTED BHXBs

In Table A1, we show the 35 Galactic BHXBs we examine in this work. We use the WATCHDOG catalogue of Tetarenko et al. (2016) for the 31 sources that were detected before 2016. We include 4 more sources detected by the Faulkes Telescopes project (Lewis et al. 2008) after 2016. In the same table, we indicate whether the BHXBs is low-(L) or high-mass (H).

APPENDIX B: NEUTRINO BACKGROUNDS

B1 Atmospheric neutrino background

The spectrum of the lower neutrino energies is dominated by the so-called conventional atmospheric background, which is due to the decay of kaons and charged pions (Gaisser et al. 2016). The best fit of the atmospheric muon neutrino flux is (Feyereisen et al. 2017):

$$\frac{d\Phi_{\nu}}{dE_{\nu}} = 2 \times 10^{-14} \left(\frac{E_{\nu}}{10 \text{ TeV}} \right)^{-3.7} \text{ GeV}^{-1} \text{ cm}^{-2} \text{ s}^{-1} \text{ sr}^{-1} \quad (\text{B1})$$

where the normalization is set by the 10 TeV ν_{μ} flux. The power-law index changes to 3.9 for neutrino energies higher than 1 PeV.

B2 Astrophysical neutrino background

The total all-flavour neutrino and anti-neutrino astrophysical spectrum was studied by the IceCube collaboration (Aartsen et al. 2015) using both track-like (muon) and shower-like (electron) events in the TeV-PeV range, between 2009 (with the 59-string configuration) and 2012 (with the full 86-string configuration). It has recently been extended to 7.5 yr of operation and the unbroken power-law best fit of the flux for the 7.5 yr sample is (Schneider 2019):

$$\frac{d\Phi_{\nu}}{dE_{\nu}} = 6.45^{+1.46}_{-0.46} \times 10^{-18} \left(\frac{E_{\nu}}{100 \text{ TeV}} \right)^{-(2.89^{+0.20}_{-0.19})}, \quad (\text{B2})$$

where the uncertainties correspond to the 1σ confidence interval and the units are the same as equation B1.

The total astrophysical muon neutrino and anti-neutrino flux was presented by the IceCube collaboration using track-like events in the neutrino energy range of 194 TeV and 7.8 PeV, between 2009 and 2015 (Aartsen et al. 2016). It has recently been updated to the almost 10 yr sample and the best fit flux is (Stettner 2019):

$$\frac{d\Phi_{\nu_{\mu}+\bar{\nu}_{\mu}}}{dE_{\nu}} = 1.44^{+0.25}_{-0.24} \times 10^{-18} \left(\frac{E_{\nu}}{100 \text{ TeV}} \right)^{-(2.28^{+0.08}_{-0.09})}, \quad (\text{B3})$$

with the same units as equation B1.

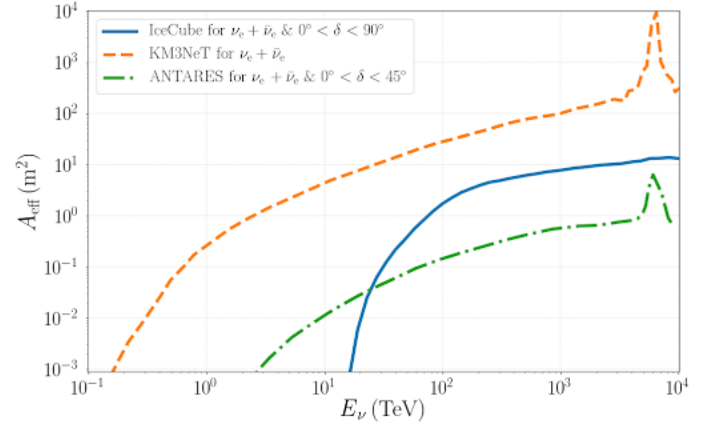


Figure C1. The effective areas of three neutrino detectors for different declination angles as shown in the legend.

B3 Diffuse neutrino spectrum

Cosmic rays in the Galactic plane interact with their ambient medium producing diffuse γ -ray emission (Ackermann et al. 2012; Abramowski et al. 2016). The γ -ray spectrum along the Galactic plane (Prodanović et al. 2007; Abdo et al. 2008) can be explained by a radial dependence of the diffusion of the CRs (Gaggero et al. 2015; Luque et al. 2022). This model, referred to as KRA_{γ} , manages to reproduce the γ -ray spectrum and makes predictions about the diffuse neutrino emission from the Galactic plane (Gaggero et al. 2015; Albert et al. 2018). The primary CR distribution is assumed to have an exponential cutoff at a certain energy.

Based on this model, IceCube and ANTARES released the upper limits at the 90 percent confidence level for the all-flavour neutrino flux (Adrián-Martínez et al. 2016; Aartsen et al. 2017b; Albert et al. 2018). According to IceCube, the best fit is achieved with an exponential cutoff at 50 PeV (KRA_{γ}^{50}), whereas a cutoff at 5 PeV (KRA_{γ}^5) is found by ANTARES.

APPENDIX C: NEUTRINO DETECTOR EFFECTIVE AREAS

To calculate the neutrino rates, we use the effective areas of IceCube, ANTARES and KM3NeT/ARCA. These are plotted in Fig. C1 for different declination angles as indicated in the legend.

APPENDIX D: CONTRIBUTION FROM INDIVIDUAL SOURCES

For the soft proton power law (top panel of Fig. D1), we see that the HMXBs Cyg X-1, MWC 656 (Aleksić et al. 2015), and SAX J1819.3-2525 (Orosz et al. 2001) are the sources that mainly contribute to the total neutrino spectrum. For the hard proton power law (bottom panel of Fig. D1), Cyg X-1 dominates the neutrino emission.

APPENDIX E: JET MODEL DEPENDENCE

E1 Neutrino flux per jet zone

In Fig. E1 we plot the total muon neutrino and antineutrino jet flux of Cyg X-1 similar to Fig. 2 but we also include the flux of each

Name	Dec (J2000)	RA (J2000)	Distance (kpc)	M_{BH} (M_{\odot})	Inclination (deg)	Companion
1A 0620-00	-00 20 44.72	06 22 44.503	1.06	6.6	51	L
XTE J1118+480	+48 02 12.6	11 18 10.80	1.7	7.3	75.0	L
SWIFT J1357.2-0933	-09 19 12.00	13 57 16.818	3.9	8.0	60.0	L
MAXI J1543-564	-56 24 48.35	15 43 17.336	5	8.0	60.0	L
XTE J1550-564	-56 28 35.0	15 50 58.78	4.4	10.4	67.4	L
4U 1630-472	-47 23 34.8	16 34 01.61	5	8.0	60.0	L
XTE J1650-500	-49 57 43.6	16 50 00.98	2.6	4.7	75.2	L
GRO J1655-40	-39 50 44.90	16 54 00.137	3.2	5.4	69	L
GX 339-4	-48 47 22.8	17 02 49.36	8	8.0	60.0	L
IGR J17091-3624	-36 24 24.	17 09 08.	5	8.0	60.0	L
GRS 1716-249	-25 01 03.4	17 19 36.93	2.4	8.0	60.0	L
XTE J1720-318	-31 45 01.25	17 19 58.994	5	8.0	60.0	L
1E 1740.7-2942	-29 44 42.6	17 43 54.83	5	8.0	60.0	L
Swift J174510.8-262411	-26 24 12.60	17 45 10.849	5	8.0	60.0	L
CXOGC J174540.0-290031	-29 00 31.0	17 45 40.03	8	8.0	60.0	L
H 1743-322	-32 14 00.60	17 46 15.608	10.4	8.0	60.0	L
XTE J1752-223	-22 20 32.782	17 52 15.095	3.5	9.6	60.0	L
Swift J1753.5-0127	-01 27 06.2	17 53 28.29	5	8.0	60.0	L
GRS 1758-258	-25 44 36.1	18 01 12.40	5	8.0	60.0	L
SAX J1819.3-2525 (V4641 Sgr)	-25 24 25.8	18 19 21.63	6.2	6.4	72.3	H
MAXI J1836-194	-19 19 12.1	18 35 43.43	5	8.0	9.5	L
XTE J1859+226	+22 39 29.4	18 58 41.58	8	10.8	60	L
XTE J1908+094	+09 23 04.90	19 08 53.077	6.5	8.0	60.0	L
SS 433	+04 58 57.9	19 11 49.57	5.5	8.0	60.0	L
GRS 1915+105	+10 56 44.8	19 15 11.55	8.6	12.4	70	L
4U 1956+350 (Cyg X-1)	+35 12 05.778	19 58 21.675	2.22	21.4	27.1	H
GS 2000+251	+25 14 11.3	20 02 49.58	2.7	8.4	60.0	L
GS 2023+338 (V404 Cyg)	+33 52 02.2	20 24 03.83	2.39	7.2	80.1	L
4U 2030+40 (Cyg X-3)	+40 57 27.9	20 32 25.78	8.3	2.4	43	H
MWC 656	+44 43 18.25	22 42 57.30	2.6	5.4	66	H
MAXI J1820+070	7.18563	275.091	2.96	9.2	63	L
MAXI J1348-630	-63.274	207.054	5.3	9.1	60	L
MAXI J1535-571	-57.23	233.832	4.1	10.4	45	L
MAXI J1828-249	-25.029	277.244	7.0	9.0	60	L

Table A1. The 35 known Galactic BHXBs we use in this work. The values of the Distance, the Mass of the black hole and the inclination are from the WATCHDOG catalogue (see [Tetarenko et al. 2016](#), and references therein) for the first 31 sources, but we use the updated values of [Miller-Jones et al. \(2021\)](#) for Cyg X-1. When the exact distance is unknown, [Tetarenko et al. \(2016\)](#) assume 5 kpc, when the mass is unknown, they assume $8 M_{\odot}$, and when the inclination is unknown, they assume 60° . We indicate these values with italics. MAXI J1820+070 ([Atri et al. 2020](#)), MAXI J1348-630 ([Belloni et al. 2020](#)), MAXI J1535-571 ([Chauhan et al. 2019](#)) and MAXI J1828-249 ([Oda et al. 2019](#)) were detected after 2016 and are not in the WATCHDOG catalogue. The last column indicates the nature of the companion, where L and H stand for low-mass and high-mass, respectively.

individual jet segment as indicated by the colourmap. The neutrino flux due to py interactions drops along the jet height following the decrease of the density of the photon field that acts as target. The neutrino flux due to pp interactions, on the other hand, drops for the first few segments because the number density of the target protons is dominated by the cold protons of the jets. The neutrino flux increases at some distance of the order of $10^6 r_g$ which is approximately the separation distance between the companion star and the compact object because at that distance the target proton density is dominated by the cold protons of the wind of the companion star. In Fig. E2 we plot the number density of the accelerated protons multiplied by

the density of the target protons and the volume. This quantity is proportional to the neutrino flux, which we show in the lower panel of the same figure.

E2 Physical processes timescales

In Fig. E3 we plot the inverse timescale of the various physical processes in the jets of Cyg X-1. The interface between the acceleration and the escape gives the maximum attainable energy. The rates of the hadronic process are at least three orders of magnitude below the

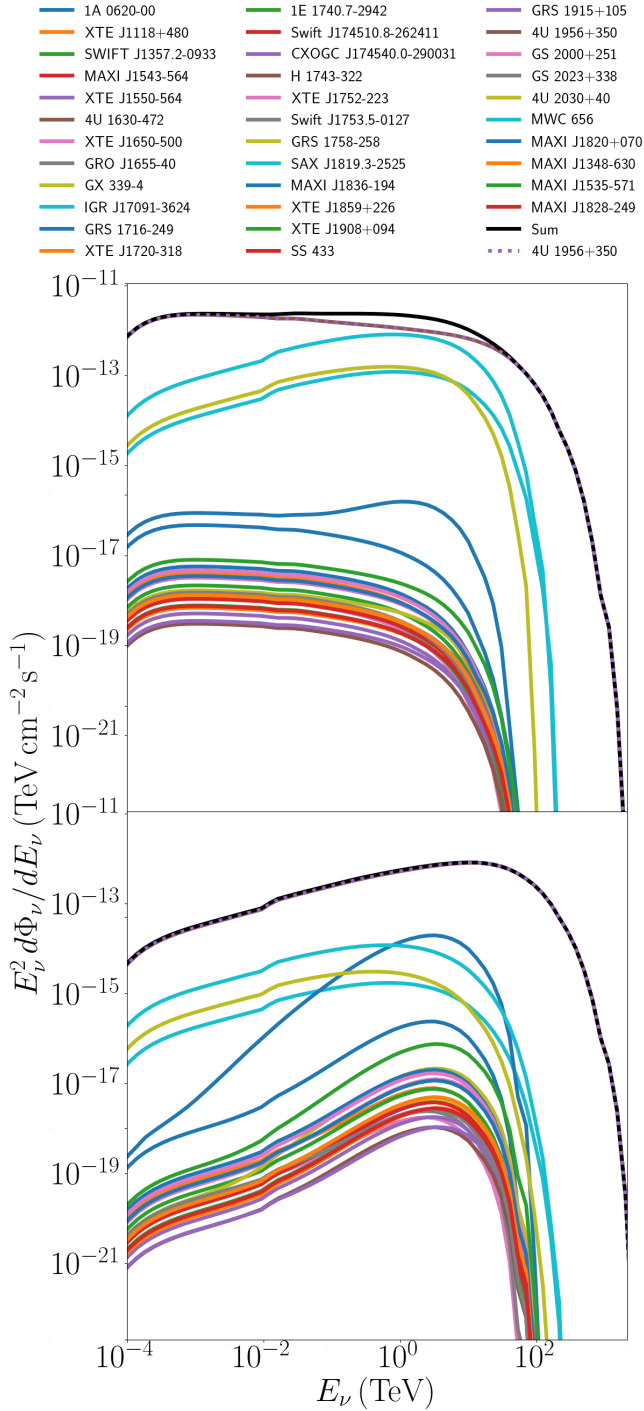


Figure D1. Contribution of all known sources to the total intrinsic $\nu_\mu + \bar{\nu}_\mu$ spectrum, assuming a soft power law of accelerated protons ($p = 2.2$) for the top figure and a hard ($p = 1.7$) for the bottom figure.

escape rate, which means that CR protons escape the jets without losing their energy due to hadronic interactions.

E3 Maximum CR energy from a HMXB

In Fig. E4, we show the inverse of the acceleration and escape timescale similar to Fig. 10 but for the case of a HMXB based on K21. For the acceleration due to magnetic reconnection, we use

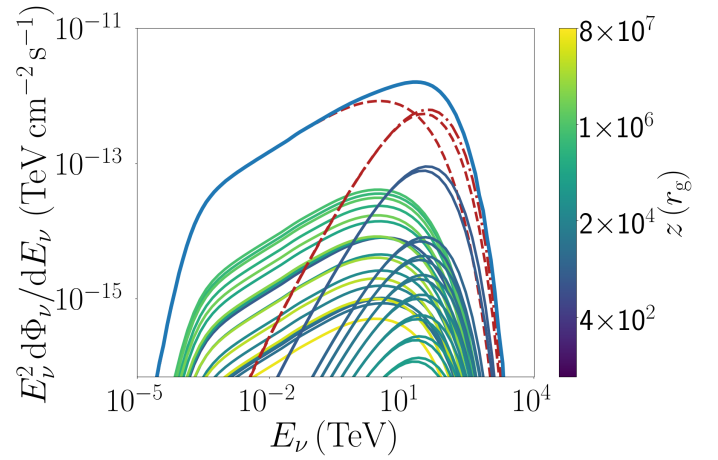


Figure E1. The intrinsic muon neutrino and antineutrino energy flux of the jets of Cyg X-1 for a proton power law with index $p = 1.7$. The dashed lines are the same as the upper left panel of Fig. 2 and the thin coloured lines correspond to individual jet zones as indicated in the colourmap.

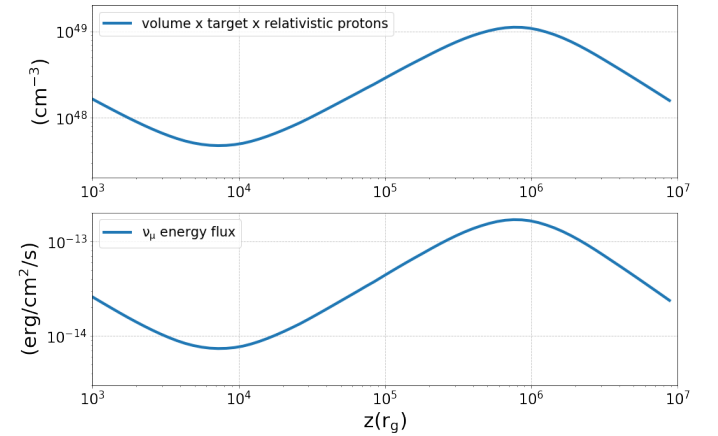


Figure E2. In the upper panel, we plot the number density of the accelerated protons multiplied by the density of the target protons and the volume of each jet segment along the jet. In the lower panel, we show the neutrino flux along the jets of Cyg X-1.

$n_e = 6 \times 10^{11} \text{ cm}^{-3}$, which is the particle number density at s_{diss} for Cyg X-1. Overall, the maximum CR energy ranges between 1 TeV and 10 PeV. See Section 5 for a more coherent discussion.

This paper has been typeset from a \LaTeX file prepared by the author.

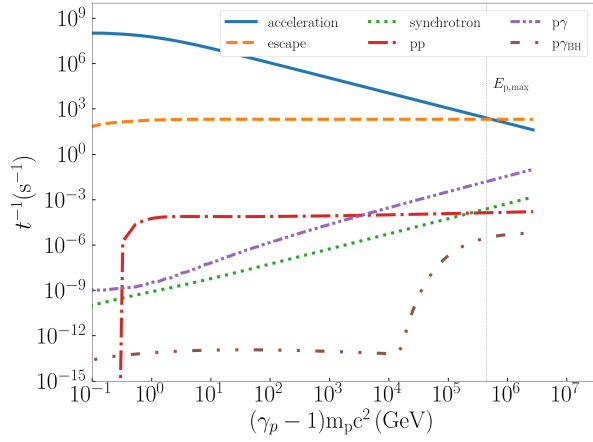


Figure E3. The inverse timescale of the physical processes at the particle acceleration region of Cyg X-1 versus the proton kinetic energy. The vertical dashed line shows the maximum proton energy.

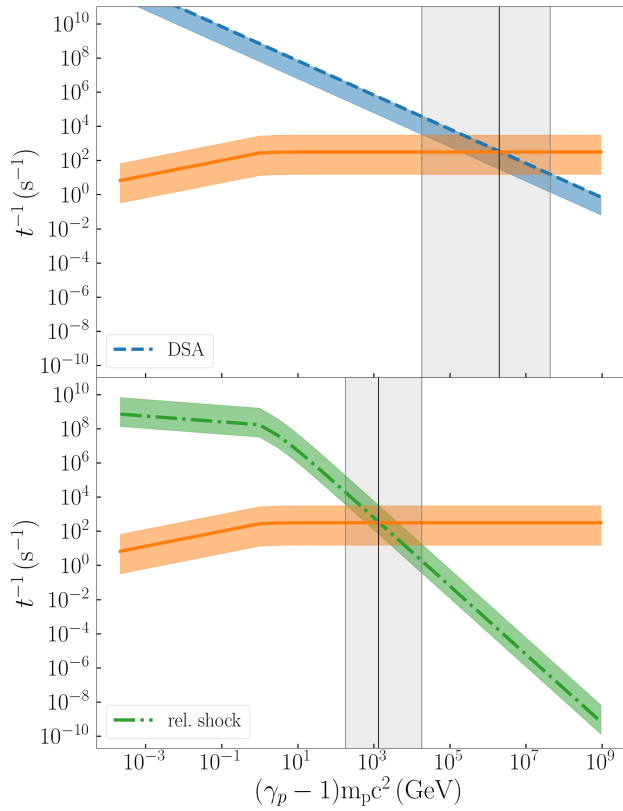


Figure E4. Similar to Fig. 10 but for HMXBs. Both mechanisms allow for maximum proton energy between 1 TeV and 10 PeV.